Small-Signal Stability Analysis and Enhancement of Virtual Admittance Control Based Grid-Forming MMC

Lei Gao, *Student Member, IEEE*, Jing Lyu, *Senior Member, IEEE*, Aolin Shi, Xiaoqiang Fu, and Xu Cai, *Senior Member, IEEE*

***Abstract*—Grid-forming modular multilevel converters (GFM-MMCs) have emerged as a promising technology for enhancing small-signal stability of power systems, particularly under weak grid conditions. Virtual admittance control has been employed for current limiting in GFM-MMCs. However, a potential challenge is that virtual admittance control could adversely affect its small-signal stability performance under weak grid condition. In this article, through the utilization of accurate impedance modeling, the control links of the virtual admittance control-based GFM-MMC are represented as virtual resistors, inductors, and capacitors. This circuit-theoretic perspective offers insights into the negative resistance characteristic that contributes to small-signal instability. Subsequently, the mechanism of small-signal instability and a method for enhancing stability are investigated using the established circuit model. Finally, the validation of the proposed method is demonstrated through simulations conducted using MATLAB/Simulink and the experimental platform of RT-LAB. These results confirm that the proposed method effectively enhances the stability of GFM-based MMC with virtual admittance control under weak grid condition, without compromising their dynamic performance.**

***Index Terms*—Equivalent circuit, grid-forming (GFM), modular multilevel converter (MMC), negative resistance, small-signal stability, virtual admittance control.**

ABBREVIATIONS

MMC	Modular multilevel converter.
HVDC	High-voltage dc.
SG	synchronous generator.
HSS	harmonic state space.
GFL	Grid-following.
GFM	Grid-forming.
VSG	Virtual synchronous generator.
PCC	Point of common coupling.
SCR	Short-circuit ratio.
LPF	Low-pass filters.
HPF	High-pass filter.
BPF	Band-pass filters.
BSF	Band-stop filters.

Symbols

$V_{\rm dc}$	DC voltage.
i_{ux}, i_{lx}	Upper and lower arm currents.
V_{gx}, I_{gx}	AC-side voltage and current.
$L_{\rm arm}$, $R_{\rm arm}$	Arm inductance and resistance.
$C_{\rm arm}$	Arm equivalent submodule capacitance.
n_{ux}, n_{lx}	Modulation functions for the upper and lower arms.
v_{cux}^{Σ}, v_{clx}^{Σ}	Arm equivalent capacitor voltages of the upper and lower arms.
$\boldsymbol{X_T}$, $\boldsymbol{U_T}$	Fourier coefficient matrices of state variables and input variables in terms of their respective harmonic components.
$\boldsymbol{A_T}$, $\boldsymbol{B_T}$	Coefficient matrices, $\boldsymbol{A_T}$ and $\boldsymbol{B_T}$ are Toeplitz matrices.
$\boldsymbol{Q_T}$	Diagonal matrix contains all the perturbation frequencies.
$\boldsymbol{i_{comabc}}$, $\boldsymbol{u_{cuabc}}$, $\boldsymbol{u_{clabc}}$, $\boldsymbol{i_{gabc}}$	Three-phase circulating current, the sum of capacitor voltages in upper and lower arms, ac-side current, respectively.
$\boldsymbol{TF_{vi}}$	Transfer function from the ac-side three-phase currents to differential-mode voltages.
$\boldsymbol{TF_{v}}$,	Transfer function from the ac-side three-phase voltages to differential-mode voltages.
$\boldsymbol{TF_{cc}}$	Transfer function from the circulating current to common-mode voltage.
$\boldsymbol{V_{gT}}$, $\boldsymbol{I_{gT}}$,	Complex phasors of the resulting perturbation voltage and current at frequency ω_T.
D_p, D_q	Active power and reactive power droop coefficients.
J_p	Virtual inertia.
H_I, H_{cc}	PI controller of current inner loop control and CCSC.
K_{ac}	Proportional coefficient of the automatic voltage regulator.

Received 1 April 2025; revised 15 July 2025 and 3 September 2025; accepted 29 September 2025. Date of publication 10 October 2025; date of current version 19 January 2026. This work was supported by the National Natural Science Foundation of China under Grant 52277195. Recommended for publication by Associate Editor H. Wu. *(Corresponding author: Jing Lyu.)*

Lei Gao, Jing Lyu, Aolin Shi, and Xu Cai are with the Key Laboratory of Control of Power Transmission and Conversion, Ministry of Education, School of Electrical Engineering, Shanghai Jiao Tong University, Shanghai 200240, China (e-mail: gaolei97@sjtu.edu.cn; lvjing@sjtu.edu.cn; slfw420@sjtu.edu.cn; xucai@sjtu.edu.cn).

Xiaoqiang Fu is with the School of Electrical Power Engineering, Shanghai University of Electric Power, Shanghai 200090, China (e-mail: fxq0301@mail.shiep.edu.cn).

Color versions of one or more figures in this article are available at https://doi.org/10.1109/TPEL.2025.3620354.

Digital Object Identifier 10.1109/TPEL.2025.3620354

H_{v1}	AC voltage middle loop control.
H_{v2}	Virtual admittance control.
K_{pac}, K_{iac}	PI controller of H_{v1}.
R_v, L_v	Virtual resistance and inductance.
K_{id}	Decoupling coefficients for the current inner loop.
K_{ccd}	Decoupling coefficients for the CCSC.
k_{vf}	Coefficient of the voltage feed-forward path.
T_d	Control delay.
$V_{sd\text{ref}}$, $V_{sq\text{ref}}$	dq-axis components of the fundamental and
$V_{ccd\text{ref}}$, $V_{ccq\text{ref}}$	second-order modulation reference voltages.
V_{sabc}, V_{ccabc}	Three-phase modulation voltages for the fundamental and second-order components.
$\boldsymbol{H_{vT}}$, $\boldsymbol{D_{qT}}$, $\boldsymbol{G_{dT}}$, $\boldsymbol{H_{ccT}}$	Topelitz matrices for ac voltage middle loop or virtual admittance control, droop control, control delay, and CCSC.
$\boldsymbol{H_{iT}}$	Topelitz matrices for the current inner loop control.
$\Delta \boldsymbol{V_{\text{diff}}}$	Differential-mode voltage matrix.
Z_g	Grid impedance.
$\boldsymbol{T}_{\text{inv}}$, $\boldsymbol{T}_p$	harmonic expansions of the Park transformation matrix and inverse Park transformation matrix.
$\boldsymbol{I}$	Identity matrix.
$\boldsymbol{T_{qdp}}$	Harmonic expansion of the park transformation matrix.
$\boldsymbol{T_{p2}}$, $\boldsymbol{T_{\text{inv2}}}$	Harmonic expansions of the double-frequency Park and inverse Park transformation matrices.

I. Introduction

MODULAR multilevel converters (MMCs) with advantages such as lower switching frequency, good controllability, and higher waveform quality, are increasingly applied in high-voltage dc (HVDC) transmission systems [1], [2]. Currently, MMCs are conventionally controlled as current sources and operated in a grid-following (GFL) manner, with synchronization realized by a phase-locked loop (PLL) [2]. GFL-based MMCs have been widely used for injecting the power into the main grid in practical engineering. However, GFL-based inverters possess several limitations, including their inability to operate in standalone mode, stability issues encountered under weak grid conditions and faulty conditions, as well as their negative impact on system inertia [3]. These limitations raise concerns regarding the reliability and security of the future power system, which is predominantly composed of power electronic converters.

To address these challenges, the existing control approach of power converters necessitates a shift from following the grid voltage to actively forming the grid voltage. From this perspective, grid-forming (GFM) technology emerges as a promising solution, enabling power converters to function as voltage sources and replicate certain characteristics of synchronous generators, particularly the emulation of the swing equation [4]. GFM-based power converters can provide a viable solution for enhancing system stability and virtual inertia in wider interconnected power networks with a high penetration of power electronics-based generation in modern HVDC transmission systems [5], [6], essentially enabling operation in weak grid conditions [7].

However, the overcurrent protection of GFM-based power converters necessitates particular attention due to their voltage source characteristics. GFM-based power converters are only capable of withstanding a few percent of overloading and two or three times their rated current within several milliseconds [4]. To overcome this critical issue and ensure the safety of the system, current limitation techniques have to be implemented. Installing additional current limiting devices (such as solid-state or superconducting fault current limiter [8], [9], bidirectional semiconductor switch [10] and current limiting reactors [11], [12]) for a massive number of GFM-based MMCs will significantly increase economic costs due to the expensive switching components. Hence, GFM-based power converters must be protected against short-circuits solely through appropriate current-limiting control strategies, while maintaining the synchronization and the connectivity to the power grids [13].

Several methods have been employed to limit the fault current during large disturbances in GFM-based power converters. One way is to switch the GFM to the GFL in case of grid faults [14]. However, this solution requires the PLL to maintain synchronization between the converter and the power grid during fault ride through process, which may induce instability issues in weak grids [14], [15]. Another current limiting method involves saturating the current reference [16], [17] in converters equipped with cascaded inner voltage and current control loops, wherein the generated current reference becomes saturated in the event of overcurrent. However, the utilization of simple current reference saturation limiting may lead to the instability if the voltage regulator loses control after the current reference saturates [18]. The third strategy for current limiting relies on virtual impedance /admittance control, enabling the adjustment of the parameters of the virtual impedance or admittance whenever the current surpasses its nominal level [18], [19]. In comparison to the second method, the third method offers the advantage of addressing overcurrent issues while maintaining the voltage source behavior behind impedance, thereby facilitating the expansion of the stability margin [4]. Furthermore, virtual impedance or virtual admittance control can be easily integrated into various control structures. It is also capable of addressing a wide range of complex operating conditions and can be flexibly adjusted to meet specific requirements [18], [19], [20].

Existing research has predominantly focused on investigating and analyzing the current limitation's capabilities by incorporating virtual impedance/admittance control for current limitation [5], [21]. Additionally, the power coupling issue, which primarily stems from the inductively dominated line impedance, can be mitigated by utilizing the virtual impedance/admittance control to reshape the equivalent total impedance [22], [23]. Virtual impedance/admittance control possesses the capability to limit fault currents and mitigate the degree of power coupling. However, the virtual resistance and virtual inductance have a contradictory effect on the small-signal stability and the current limitation's capabilities [4]. The negative resistance may be still introduced within 200 Hz in the GFM-based MMC with virtual impedance/admittance control [24], [25]. Instability can still

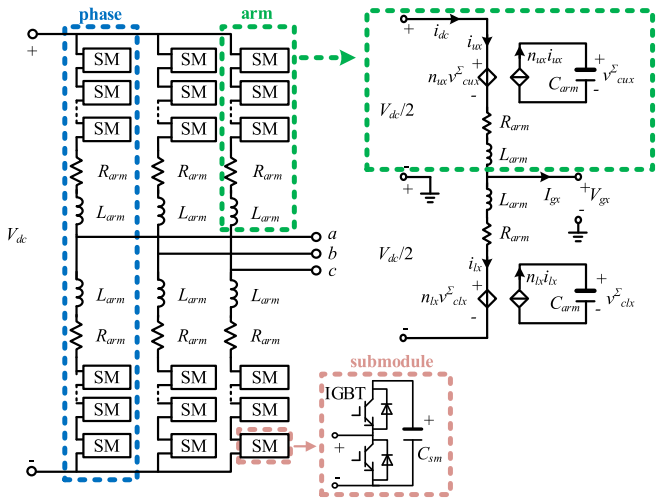

Fig. 1. Basic topology of the MMC.

arise as a result of the negative resistance being triggered within specific frequency ranges [26]. The interaction between reactive power control and virtual impedance/admittance control may also deteriorate system stability [26].

Recently, the majority of studies have focused on analyzing two-level converters [27], [28], while overlooking the multi-harmonic characteristics and nonlinearities introduced by the converter dynamics of MMCs. The conventional state-space method, based on eigenvalue analysis, requires small-signal modeling of the entire MMC system [29]. It assesses stability by evaluating the damping ratios of system eigenvalues to identify key factors influencing stability but it cannot reveal the negative resistance's mechanism. Pan et al. [26] and Nahalparvari et al. [30] both focus on the impedance modeling and instability analysis of GFM-MMCs, but fails to reveal the physical essence of negative resistance introduced by virtual impedance/admittance control. Accurate impedance modeling is the foundation for negative resistance analysis. In this article, the harmonic state space (HSS) methodology [31], [32] has been employed for the initial derivation of theoretical ac-side impedance models for GFM-MMCs. These models have been subsequently validated through frequency scanning simulations. On this basis, control links and factors with minimal impact on negative resistance characteristics have been neglected. The reactive power control, virtual admittance control, and current inner loop control of MMCs are represented as equivalent circuit elements, including virtual resistors, inductors, capacitors, and controlled voltage sources [33], [34], thereby facilitating the understanding of the nature of negative resistance from a circuit-theoretic perspective. Furthermore, the small-signal instability mechanism of virtual admittance control-based GFM-MMCs under weak grid conditions is investigated using the established circuit model. Subsequently, a small-signal stability enhancing approach is proposed based on the instability mechanism analysis. Ultimately, the validation of the proposed small-signal stability enhancement method is demonstrated through simulations utilizing MATLAB/Simulink and the experimental platform of RT-LAB.

Compared to the state-of-the-art in the literature, the key contributions of this article are outlined as follows:

1) *Novel Circuit-Theoretic Representation:* Based on the accurate ac-side impedance modeling, the control links of the virtual admittance control-based GFM-MMC are visualized as *RLC* circuit including the virtual resistors, inductors, and capacitors. It provides a comprehensive circuit-theoretic representation of the system's control dynamics from a circuit-theoretic perspective.
2) *Insight into Negative Resistance Mechanism:* The circuit-theoretic perspective elucidates the negative resistance nature introduced by the interaction between virtual admittance control and current inner loop control, offering a clear understanding of the underlying mechanisms that contribute to small-signal instability.
3) *Innovative Active Damping Strategy:* Based on the mechanism of small-signal instability, an active damping strategy is proposed that effectively balances small-signal stability and overcurrent suppression. This is achieved by incorporating low-pass filters into the voltage feedforward and active damping into the cross-decoupling terms, respectively, ensuring robust performance during fault ride-through scenarios without compromising dynamic response.

The rest of this article is organized as follows. In Section II, the ac-side impedance model of MMC is established and subsequently verified. In Section III, the control links of MMC are portrayed as virtual impedance from a circuit-theoretic perspective. In Sections IV and V, the instable mechanism of GFM-based MMC with virtual admittance control is elaborated, and a small-signal stability enhancement method is proposed. In Section VI, the simulation and experimental results are presented. Finally, Section VII concludes this article.

II. AC-Side Impedance Modeling of MMC

A. Topology and Control of MMC

In this article, the average-value model of the MMC is adopted, assuming equal capacitor voltages across submodule capacitors. The equivalent circuit of one leg of MMC is depicted in Fig. 1. $V_{\rm dc}$ denotes the dc voltage. i_{ux} and i_{lx} are the upper and lower arm currents, respectively. V_{gx} and I_{gx} are the ac-side voltage and current, respectively. Additionally, $L_{\rm arm}$ and $R_{\rm arm}$ are the arm inductance and resistance, respectively, $C_{\rm arm}$ represents the arm equivalent submodule capacitance, n_{ux} and n_{lx} are the modulation functions for the upper and lower arms. v^{Σ}_{cux} and v^{Σ}_{clx} are the arm equivalent capacitor voltages of the upper and lower arms, respectively. The subscript $x = a, b, c$ indicates three-phase configuration.

The control diagram of the MMC is depicted in Fig. 2, which encompassing the active power outer control, ac voltage middle loop control or virtual admittance control, ac current inner loop, and second-order circulating current suppressing control (CCSC).

In Fig. 2, subscripts d and q denote the components in the dq axis rotating coordinate system and subscripts a, b, and c represent the components in the abc stationary coordinate system. D_p and D_q represent the active power and reactive power droop coefficients, respectively. The active power outer

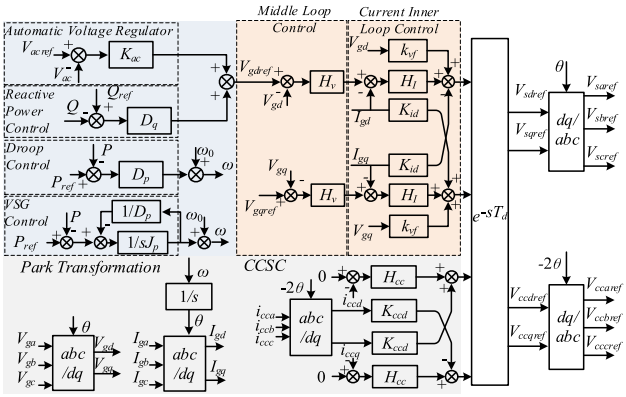

Fig. 2. Control diagram of MMC.

control is virtual synchronous generator (VSG) control if the virtual inertia J_p is considered. The active power outer control is droop control if J_p is not considered. In this article, the droop control is adopted. The active power outer loop with the droop coefficient is integrated to obtain the Park transformation angle. H_I, and H_{cc} represent the current inner loop control and CCSC, respectively. $H_I = K_{pi}+K_{ii}/s$. $K_{\rm ac}$ represents the proportional coefficient of the automatic voltage regulator. H_v represents the transfer functions of the PI controllers for the ac voltage middle loop control or virtual admittance control, expressed as H_{v1} in (1) and H_{v2} in (2) respectively. $K_{\rm pac}$ and $K_{\rm iac}$ represent the PI parameters, respectively. R_v and L_v represent the virtual resistance and inductance, respectively,

$$H_{v1} = K_{\rm pac} + \frac{K_{\rm iac}}{s}, H_{v1} \text{ is AC voltage control} \tag{1}$$

$$H_{v2} = \frac{1}{R_v + sL_v}, H_{v2} \text{ is virtual admittance control.} \tag{2}$$

K_{id} and K_{ccd} are the decoupling coefficients for the current inner loop and CCSC, respectively. $K_{id} = k_{dec}\omega_0 L_{\rm arm}/2$. k_{vf} denotes the coefficient of the voltage feed-forward path, and T_d represents the control delay. $V_{sd\rm ref}$, $V_{sq\rm ref}$, $V_{ccd\rm ref}$, and $V_{ccq\rm ref}$ are the dq-axis components of the fundamental and second-order modulation reference voltages, respectively. V_{sabc} and V_{ccabc} represent the three-phase modulation voltages for the fundamental and second-order components, respectively.

B. Impedance Modeling and Validation

The MMC exhibits complex internal dynamics due to its multiharmonic interactions (e.g., circulating currents, capacitor voltage ripple, and sideband harmonics). Traditional state-space modeling, which assumes a single-frequency operating point, fails to capture these cross-frequency couplings, leading to inaccuracies in stability assessment, particularly under weak grid conditions. In contrast, the HSS method explicitly models harmonic components and their interactions by representing state variables and control dynamics in a Fourier-series-based state-space framework. According to [31], by considering the internal dynamics of MMC, the small-signal HSS model of MMC can be obtained as

$$s\boldsymbol{X_T} = (\boldsymbol{A_T} - \boldsymbol{Q_T})\,\boldsymbol{X_T} + \boldsymbol{B_T}\boldsymbol{U_T} \tag{3}$$

where $\boldsymbol{X_T}$ and $\boldsymbol{U_T}$ represent the Fourier coefficient matrices that express the state variables and input variables in terms of their respective harmonic components. $\boldsymbol{X_T}$, $\boldsymbol{U_T}$ are given in (4) and (5), respectively. $\boldsymbol{i_{comabc}}$, $\boldsymbol{u_{cuabc}}$, $\boldsymbol{u_{clabc}}$, $\boldsymbol{i_{gabc}}$ represent three-phase circulating current, the sum of capacitor voltages in upper and lower arms, ac-side current, respectively. V_T represents the disturbance component. The prefix Δ represents small-signal components

$$\begin{aligned}
\boldsymbol{X_T} &= [\Delta\boldsymbol{i_{comabc}}, \Delta\boldsymbol{u_{cuabc}}, \Delta\boldsymbol{u_{clabc}}, \Delta\boldsymbol{i_{gabc}}]^T \\
\Delta\boldsymbol{i_{comabc}} &= \text{diag}[\Delta\boldsymbol{i_{coma}}, \Delta\boldsymbol{i_{comb}}, \Delta\boldsymbol{i_{comc}}]_{3\times3} \\
\Delta\boldsymbol{i_{comx}} &= [\Delta\boldsymbol{i_{comx}}(-h\omega_1), \cdots, \Delta\boldsymbol{i_{comx}}(dc), \cdots, \\
&\quad \Delta\boldsymbol{i_{comx}}(h\omega_1)]^T \\
\Delta\boldsymbol{u_{cuabc}} &= \text{diag}\,[\Delta\boldsymbol{u_{cua}}, \Delta\boldsymbol{u_{cub}}, \Delta\boldsymbol{u_{cuc}}]_{3\times3} \\
\Delta\boldsymbol{u_{cux}} &= [\Delta\boldsymbol{u_{cux}}(-h\omega_1), \cdots, \Delta\boldsymbol{u_{cux}}(dc), \cdots, \\
&\quad \Delta\boldsymbol{u_{cux}}(h\omega_1)]^T \\
\Delta\boldsymbol{u_{clabc}} &= \text{diag}[\Delta\boldsymbol{u_{cla}}, \Delta\boldsymbol{u_{clb}}, \Delta\boldsymbol{u_{clc}}]_{3\times3} \\
\Delta\boldsymbol{u_{clx}} &= [\Delta\boldsymbol{u_{clx}}(-h\omega_1), \cdots, \Delta\boldsymbol{u_{clx}}(dc), \cdots, \\
&\quad \Delta\boldsymbol{u_{clx}}(h\omega_1)]^T \\
\Delta\boldsymbol{i_{gabc}} &= \text{diag}[\Delta\boldsymbol{i_{ga}}, \Delta\boldsymbol{i_{gb}}, \Delta\boldsymbol{i_{gc}}]_{3\times3} \\
\Delta\boldsymbol{i_{gx}} &= [\Delta\boldsymbol{i_{gx}}(-h\omega_1), \cdots, \Delta\boldsymbol{i_{gx}}(dc), \cdots, \\
&\quad \Delta\boldsymbol{i_{gx}}(h\omega_1)]^T, \boldsymbol{x} = \boldsymbol{a}, \boldsymbol{b}, \boldsymbol{c}
\end{aligned} \tag{4}$$

$$\begin{aligned}
\boldsymbol{U_T} &= [\boldsymbol{O}_{2h+1}, \boldsymbol{O}_{2h+1}, \boldsymbol{O}_{2h+1}, \boldsymbol{O}_{2h+1}, \boldsymbol{O}_{2h+1}, \boldsymbol{O}_{2h+1}, \\
&\quad \boldsymbol{O}_{2h+1}, \boldsymbol{O}_{2h+1}, \boldsymbol{O}_{2h+1}, \boldsymbol{U_{Ta}}, \boldsymbol{U_{Tb}}, \boldsymbol{U_{Tc}}]^T \\
\boldsymbol{U_{Ta}} &= [0, \cdots V_T, \cdots, 0]^T_{(2h+1)}, \boldsymbol{U_{Tb}} \\
&= \left[0, \cdots V_T e^{-j\frac{2}{3}\pi}, \cdots, 0\right]^T_{(2h+1)} \\
\boldsymbol{U_{Tc}} &= \left[0, \cdots V_T e^{j\frac{2}{3}\pi}, \cdots, 0\right]^T_{(2h+1)}.
\end{aligned} \tag{5}$$

It is noted that the diagonal matrix $\boldsymbol{Q_T}$ contains all the perturbation frequencies that are defined in (6), which means that this model considers all the frequency coupling effects

$$\begin{aligned}
\boldsymbol{Q_T} &= \text{diag}\,[\boldsymbol{W_T}, \boldsymbol{W_T}, \boldsymbol{W_T}, \boldsymbol{W_T}, \boldsymbol{W_T}, \boldsymbol{W_T}, \boldsymbol{W_T}, \boldsymbol{W_T}, \\
&\quad \boldsymbol{W_T}, \boldsymbol{W_T}, \boldsymbol{W_T}, \boldsymbol{W_T}] \\
\boldsymbol{W_T} &= \text{diag}\,[j(\omega_T - h\omega_0), \cdots, j\omega_T, \cdots, j(\omega_T + h\omega_0)].
\end{aligned} \tag{6}$$

According to the HSS theory, the Topelitz matrix of a linear controller is a diagonal matrix, and the transfer function of the linear controller can be frequency shifted along the diagonal line. Considering the first four harmonics [31], [32], the Topelitz matrix$\boldsymbol{H_{iT}}$for the current inner loop control is expressed as (7).Meanwhile, the Topelitz matrices$\boldsymbol{H_{vT}}$,$\boldsymbol{D_{qT}}$,$\boldsymbol{G_{dT}}$and$\boldsymbol{H_{ccT}}$for

the ac voltage middle loop or virtual admittance control, droop control, control delay, and CCSC are given as

$$\boldsymbol{H_{iT}}=\begin{bmatrix}\boldsymbol{H_I} & \boldsymbol{O}_{(2h+1)\times(2h+1)}\\ \boldsymbol{O}_{(2h+1)\times(2h+1)} & \boldsymbol{H_I}\end{bmatrix}$$
$$\boldsymbol{H_I}=\text{diag}\left[H_I(s-jh\omega_1),\cdots,H_I(s),\cdots,H_I(s+jh\omega_1)\right] \tag{7}$$

$$\boldsymbol{H_{vT}}=\begin{bmatrix}\boldsymbol{H_v} & \boldsymbol{O}_{(2h+1)\times(2h+1)}\\ \boldsymbol{O}_{(2h+1)\times(2h+1)} & \boldsymbol{H_v}\end{bmatrix}$$
$$\boldsymbol{H_v}=\text{diag}\left[H_v(s-jh\omega_1),\cdots,H_v(s),\cdots,H_v(s+jh\omega_1)\right] \tag{8}$$

$$\boldsymbol{D_{qT}}=\begin{bmatrix}\boldsymbol{D_q} & \boldsymbol{O}_{(2h+1)\times(2h+1)}\\ \boldsymbol{O}_{(2h+1)\times(2h+1)} & \boldsymbol{D_q}\end{bmatrix}$$
$$\boldsymbol{D_q}=\text{diag}\left[D_q(s-jh\omega_1),\cdots,D_q(s),\cdots,D_q(s+jh\omega_1)\right] \tag{9}$$

$$\boldsymbol{G_{dT}}=\begin{bmatrix}\boldsymbol{G_d} & \boldsymbol{O}_{(2h+1)\times(2h+1)}\\ \boldsymbol{O}_{(2h+1)\times(2h+1)} & \boldsymbol{G_d}\end{bmatrix}$$
$$\boldsymbol{G_d}=\text{diag}\left[G_d(s-jh\omega_1),\cdots,G_d(s),\cdots,\right.$$
$$\left.G_d(s+jh\omega_1)\right],G_d=e^{-sTd} \tag{10}$$

$$\boldsymbol{H_{ccT}}=\begin{bmatrix}\boldsymbol{H_{cc}} & \boldsymbol{O}_{(2h+1)\times(2h+1)}\\ \boldsymbol{O}_{(2h+1)\times(2h+1)} & \boldsymbol{H_{cc}}\end{bmatrix}$$
$$\boldsymbol{H_{cc}}=\text{diag}\left[H_{cc}(s-jh\omega_1),\cdots,H_{cc}(s),\cdots,H_{cc}(s+jh\omega_1)\right]. \tag{11}$$

For the active power droop control, the small-signal form of active power is expressed as (12). The quantity with a subscript of "0" represents the steady-state value of voltage and current

$$\Delta P=\begin{bmatrix}I_{gd0} & I_{gq0}\end{bmatrix}\begin{bmatrix}\Delta V_{gd}\\ \Delta V_{gq}\end{bmatrix}+\begin{bmatrix}V_{gd0} & V_{gq0}\end{bmatrix}\begin{bmatrix}\Delta I_{gd}\\ \Delta I_{gq}\end{bmatrix}. \tag{12}$$

Then, the expression of $\Delta\theta$ is derived as

$$\Delta\theta=\frac{1}{s}\left(\frac{-\Delta P}{D_p+sJ_p}\right). \tag{13}$$

For the reactive power droop control, the small-signal form of the reactive power expression is as shown in

$$\Delta Q=\begin{bmatrix}-I_{gq0} & I_{gd0}\end{bmatrix}\begin{bmatrix}\Delta V_{gd}\\ \Delta V_{gq}\end{bmatrix}+\begin{bmatrix}V_{gq0} & -V_{gd0}\end{bmatrix}\begin{bmatrix}\Delta I_{gd}\\ \Delta I_{gq}\end{bmatrix}. \tag{14}$$

Then, the reference of the d-axis voltage $\Delta V_{gd\text{ref}}$ can be derived as (15) and $\Delta V_{ac}=\sqrt{V_{gd}^2+V_{gq}^2}$. The reference of the dq-axis currents can be written as (16). Therefore, the dq-axis voltages can be derived as

$$\Delta V_{gd\text{ref}}=-D_q\Delta Q+K_{\text{ac}}(-\Delta V_{\text{ac}}) \tag{15}$$

$$\begin{bmatrix}\Delta I_{gd\text{ref}}\\ \Delta I_{gq\text{ref}}\end{bmatrix}=\begin{bmatrix}H_v & \\ & H_v\end{bmatrix}\begin{bmatrix}\Delta V_{gd\text{ref}}-\Delta V_{gd}\\ \Delta V_{gq\text{ref}}-\Delta V_{gq}\end{bmatrix} \tag{16}$$

$$\begin{bmatrix}\Delta V_{sd}\\ \Delta V_{sq}\end{bmatrix}=H_I\begin{bmatrix}\Delta I_{gd\text{ref}}-\Delta I_{gd}\\ \Delta I_{gq\text{ref}}-\Delta I_{gq}\end{bmatrix}$$
$$+k_{vf}\begin{bmatrix}\Delta V_{gd}\\ \Delta V_{gq}\end{bmatrix}-K_{id}\begin{bmatrix}\Delta I_{gd}\\ \Delta I_{gq}\end{bmatrix}. \tag{17}$$

The differential-mode voltage matrix $\Delta\boldsymbol{V_{\text{diff}}}$ is derived as

$$\Delta\boldsymbol{V}_{\text{diff}}=\boldsymbol{T}_{\text{inv}}T_d\left\{\begin{bmatrix}\Delta V_{sd}\\ \Delta V_{sq}\end{bmatrix}+H_I\begin{bmatrix}\Delta I_{gd}\\ \Delta I_{gq}\end{bmatrix}-Z_g\begin{bmatrix}\Delta I_{gd}\\ \Delta I_{gq}\end{bmatrix}\right\}\boldsymbol{T_p} \tag{18}$$

where $Z_g$is the grid impedance.$\boldsymbol{T}_p$ and$\boldsymbol{T}_{\text{inv}}$represent the harmonic expansions of the Park transformation matrix and inverse Park transformation matrix, respectively. In (18), thedq-to-abc transformation is fully compatible with the HSS method. The Park transformation matrices($\boldsymbol{T_p}$,$\boldsymbol{T_{\text{inv}}}$)are expanded harmonically to preserve frequency coupling, ensuring seamless integration with the HSS framework. Toplitz expansion of Park's transformation matrix$\boldsymbol{T}_p$is given as follows:

$$\boldsymbol{T_p}=\frac{2}{3}\begin{bmatrix}\boldsymbol{A}_{\cos\boldsymbol{a}} & \boldsymbol{A}_{\cos\boldsymbol{b}} & \boldsymbol{A}_{\cos\boldsymbol{c}}\\ -\boldsymbol{A}_{\sin\boldsymbol{a}} & -\boldsymbol{A}_{\sin\boldsymbol{b}} & -\boldsymbol{A}_{\sin\boldsymbol{c}}\end{bmatrix} \tag{19}$$

where$\boldsymbol{A_{\cos a}},\boldsymbol{A_{\cos b}},\boldsymbol{A_{\cos c}}$ are Toplitz expansion of cosθ, cos(θ-2/3π), cos(θ+2/3π), and$\boldsymbol{A_{\sin a}},\boldsymbol{A_{\sin b}},\boldsymbol{A_{\sin c}}$ are Toplitz expansion of $sin\theta$, sin(θ-2/3π), sin(θ + 2/3π), respectively. $\boldsymbol{A_{\cos b}}$ is expressed as (20). Similarly, we can obtain$\boldsymbol{A_{\cos a}},\boldsymbol{A_{\cos c}},\boldsymbol{A_{\sin a}}$, $\boldsymbol{A_{\sin b}},\boldsymbol{A_{\sin c}}$ and define Park's inverse transformation $\boldsymbol{T}_{\text{inv}}$

$$\boldsymbol{A_{\cos b}}=\begin{bmatrix}0 & \frac{1}{2}e^{j\frac{2}{3}\pi} & & & \\ \frac{1}{2}e^{-j\frac{2}{3}\pi} & 0 & \frac{1}{2}e^{j\frac{2}{3}\pi} & & \\ & \ddots & \ddots & \ddots & \\ & & \frac{1}{2}e^{-j\frac{2}{3}\pi} & 0 & \frac{1}{2}e^{j\frac{2}{3}\pi}\\ & & & \frac{1}{2}e^{-j\frac{2}{3}\pi} & 0\end{bmatrix}. \tag{20}$$

Finally, the transfer functions can be derived for the relationship between the ac-side three-phase currents and voltages as well as the transfer function for the relationship between the circulating current and common-mode voltage, which are given as follows:

$$\begin{aligned}\boldsymbol{TF_{vi}}=&k_{vf}\boldsymbol{T_{\text{inv}}G_{dT}}Z_g\boldsymbol{T_p}-\boldsymbol{T_{\text{inv}}G_{dT}}K_{id}\boldsymbol{T_pT_{\text{inv}}T_p}\\&-\boldsymbol{T_{\text{inv}}G_{dT}H_{iT}H_{vT}}Z_g\boldsymbol{T_p}-\boldsymbol{T_{\text{inv}}G_{dT}H_{iT}T_p}\\&-\boldsymbol{T_{\text{inv}}G_{dT}H_{iT}H_{vT}D_{qT}}(\boldsymbol{I}+Z_g)\boldsymbol{T_p}\\&-2\boldsymbol{T_{\text{inv}}G_{dT}}\boldsymbol{\Delta}\theta\boldsymbol{T_p}\end{aligned} \tag{21}$$

$$\begin{aligned}\boldsymbol{TF_v}=&k_{vf}\boldsymbol{T_{\text{inv}}G_{dT}T_p}-\boldsymbol{T_{\text{inv}}G_{dT}H_{iT}H_{vT}T_p}\\&-\boldsymbol{T_{\text{inv}}G_{dT}H_{iT}H_{vT}K_{qT}T_p}\end{aligned} \tag{22}$$

$$\boldsymbol{TF_{cc}}=-\boldsymbol{T_{\text{inv2}}G_{dT}H_{ccT}T_{p2}}+3\boldsymbol{T_{\text{inv2}}G_{dT}}\Delta\theta\boldsymbol{T_p} \tag{23}$$

where $\boldsymbol{TF_{vi}}$ represents the transfer function from the ac-side three-phase currents to differential-mode voltages. $\boldsymbol{TF_v}$ represents the transfer function from the AC-side three-phase voltages to differential-mode voltages. $\boldsymbol{TF_{cc}}$ represents the transfer function from the circulating current to common-mode voltage. $\boldsymbol{I}$ is the identity matrix. $\boldsymbol{T_{p2}}$ and $\boldsymbol{T_{\text{inv2}}}$ represent the harmonic expansions of the double-frequency Park and inverse Park transformation matrices, respectively. $\boldsymbol{T_{p2}}$ and $\boldsymbol{T_{\text{inv2}}}$ can be defined similar as $\boldsymbol{T}_p$ and $\boldsymbol{T}_{\text{inv}}$. The matrices $\boldsymbol{A_T}$ and $\boldsymbol{B_T}$ of the small-signal HSS model of MMC can be derived after the definition of these

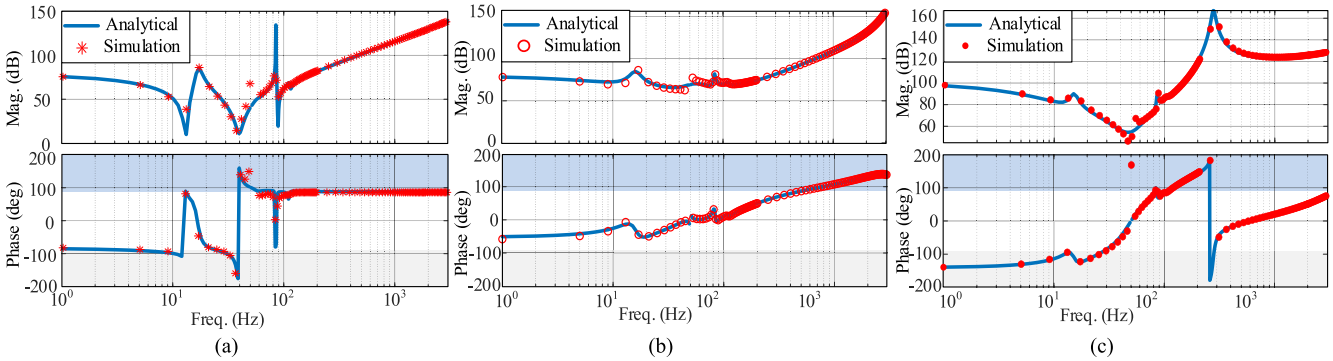

Fig. 3. Verification of MMC impedance model. (a) Only with droop control. (b) With droop control, AC voltage middle loop control and current inner loop. (c) With droop control, virtual admittance control and current inner loop.

transfer functions [31], [32]. After obtaining the small-signal HSS model of MMC, the ac-side small-signal impedance of the MMC can be obtained as

$$\boldsymbol{Z}_{\mathbf{MMC}}(j\omega_T) = -\frac{\boldsymbol{V}_{\boldsymbol{gT}}}{\boldsymbol{I}_{\boldsymbol{gT}}} \tag{24}$$

where the bold letters $\boldsymbol{V}_{\boldsymbol{gT}}$ and $\boldsymbol{I}_{\boldsymbol{gT}}$ are the complex phasors of the resulting perturbation voltage and current at frequency ω_T. Additionally, the perturbation voltage $\boldsymbol{V}_{\boldsymbol{gT}}$ is expressed as

$$\boldsymbol{V}_{\boldsymbol{gT}} = \boldsymbol{U}_{\boldsymbol{T}} + Z_g \boldsymbol{I}_{\boldsymbol{gT}} \tag{25}$$

where the perturbation input voltage $\boldsymbol{U}_{\boldsymbol{T}}$ is predefined, and the resulting perturbation current $\boldsymbol{I}_{\boldsymbol{gT}}$ can be solved as a function of the perturbation input voltage $\boldsymbol{U}_{\boldsymbol{T}}$ based on the small-signal HSS model of the MMC.

Subsequently, to validate the established impedance models, a simulation model of a three-phase grid-connected MMC was constructed to perform frequency scanning. The validation results are presented in Fig. 3, where the solid blue curve and red dots represent the impedances obtained from the theoretical models and frequency scanning, respectively. As can be observed from Fig. 3, the theoretical models align well with the frequency scanning curve, thus verifying the accuracy of the theoretical impedance models. Fig. 3(a) is the impedance model verification of MMC only with the active power outer control. Based on Fig. 3(a) and (b) is the impedance model verification of MMC with the droop control, ac voltage middle loop control and current inner loop control. Based on Fig. 3(b), the ac voltage middle loop control is substituted by the virtual admittance control in Fig. 3(c).

III. Equivalent Circuit of MMC's Control Dynamics

A. Model Simplification

According to Fig. 3, if only the power outer-loop control (i.e., the P-θ and Q-U scheme) is employed while the current inner-loop control and virtual admittance control are neglected, there would be no oscillatory instability issues for GFM-based MMC under weak grid conditions, as shown in Fig. 4(a). However, when the virtual admittance control and current inner-loop control are implemented, the negative resistance is observed in

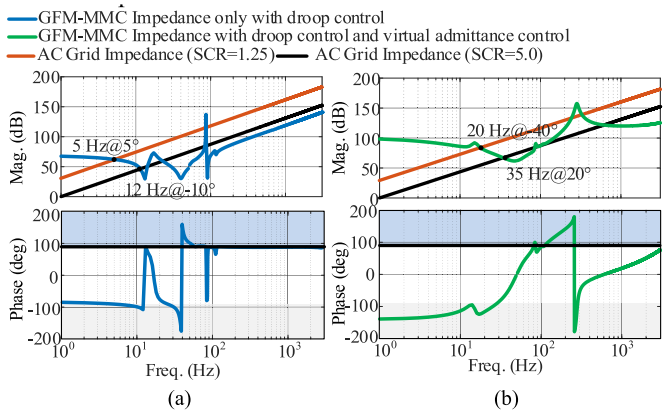

Fig. 4. MMC impedances of different controls under conditions of weak and strong AC grid. (a) GFM-MMC Impedance only with droop control. (b) GFM-MMC Impedance with droop control, virtual admittance control and current inner loop control.

the sequence impedance within the 1–30 Hz range, making the system more prone to oscillatory stability problems in weak grid scenarios, as shown in Fig. 4(b). Based on Fig. 4, to reveal the circuit essence of negative resistance, the control links with less impact on MMC impedance would be first simplified in this section.

According to the impedance sensitivity analysis, it is demonstrated that the harmonic orders, active power outer-loop control, and automatic voltage regulator have minor influences on the impedance characteristics of the MMC. Fig. 5 are the MMC impedance Bode plots affected by harmonic orders, automatic voltage regulator and active power control. In Fig. 5, the phase response in the Bode plot indicates.

1) 90° to 180° phase range corresponds to the inductive negative-resistance region.
2) −90° to −180° phase range represents the capacitive negative-resistance region.

Fig. 5(a) is the impact of harmonic order on MMC impedance. The impedance characteristics of the MMC remain nearly unchanged under varying harmonic orders, which confirming that the negative-resistance is hardly unaffected by harmonic orders. Fig. 5(b) is the effect of active power outer-loop control (D_p).

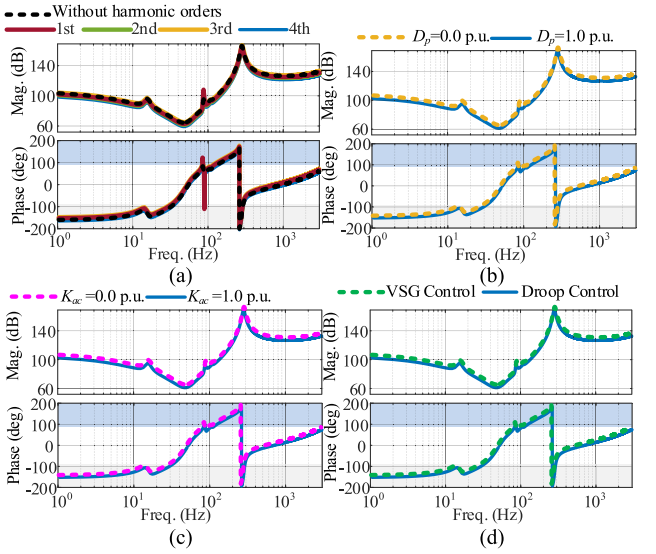

Fig. 5. MMC impedance characteristic affected by harmonic orders, automatic voltage regulator and active power control. (a) Harmonic orders. (b) Active power control. (c) Automatic voltage regulator. (d) VSG or droop control.

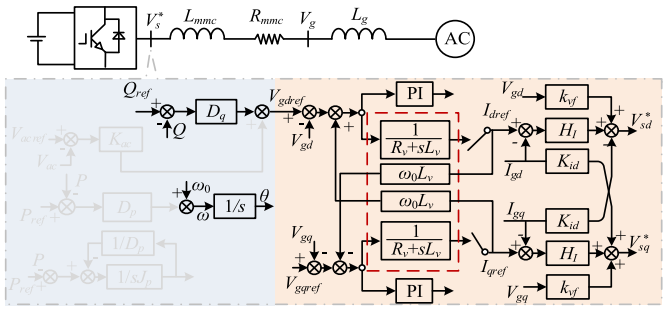

Fig. 6. Simplified topology and control of GFM-based MMC.

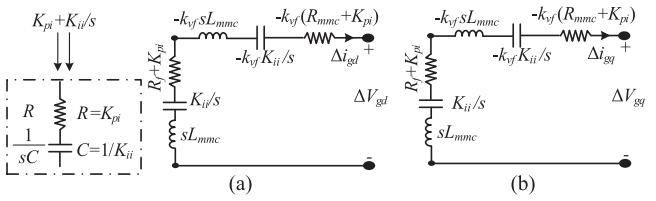

Fig. 7. Equivalent circuit of current inner loop control. (a) *d*-axis. (b) *q*-axis.

When $D_p = 0$ (i.e., without active power outer-loop control and without VSG control), the MMC impedance profile shows negligible variation. The negative-resistance region remains unchanged, indicating minimal influence from active power outer-loop control. Fig. 5(c) is the influence of automatic voltage regulator ($K_{\rm ac}$). With $K_{\rm ac} = 0$ (i.e., disabled automatic voltage regulator), the MMC impedance curve exhibits unchanged. The negative-resistance characteristics are not affected with automatic voltage regulator. Fig. 5(d) is the influence of droop or VSG control. With $J_p = 0$ (i.e., disabled VSG control), the MMC impedance curve exhibits unchanged. The damping coefficient and virtual inertia may primarily affect impedance near the fundamental frequency, with negligible impact on the studied frequency range (1–30 Hz). Thus, these factors would be omitted.

In summary, the harmonic orders, automatic voltage regulator and active power control have rarely influence on the negative resistance, as shown in Fig. 5. It also should be pointed out that these factors will not affect the MMC impedance even if the steady-state operating points change. Therefore, the equivalent circuits of these links are neglected in this section. To reveal the negative resistance' nature of GFM-based MMC, the topology and control of MMC can be simplified as Fig. 6. $R_{\rm mmc} = R_{\rm arm}/2$ and $L_{\rm mmc} = L_{\rm arm}/2$.

B. Equivalent Circuit of MMC Only With Current Inner Loop Control

Ignoring the influence of the outer loop control, $\Delta I_{d\rm ref}$ and $\Delta I_{q\rm ref}$ are set to 0 in Fig. 6. The relationship between voltage and current can be expressed as

$$\begin{bmatrix}\Delta V_{gd}\\ \Delta V_{gq}\end{bmatrix} = -\begin{bmatrix}H_I(s) & 0\\ 0 & H_I(s)\end{bmatrix}\begin{bmatrix}\Delta I_{d\rm ref}-\Delta I_{gd}\\ \Delta I_{q\rm ref}-\Delta I_{gq}\end{bmatrix}$$
$$-\begin{bmatrix}R_{\rm mmc}+sL_{\rm mmc} & -\omega_0 L_{\rm mmc}\\ \omega_0 L_{\rm mmc} & R_{\rm mmc}+sL_{\rm mmc}\end{bmatrix}\begin{bmatrix}\Delta I_{gd}\\ \Delta I_{gq}\end{bmatrix}$$
$$+\begin{bmatrix}k_{vf} & 0\\ 0 & k_{vf}\end{bmatrix}\begin{bmatrix}\Delta V_{gd}\\ \Delta V_{gq}\end{bmatrix}+k_{dec}\begin{bmatrix}0 & -\omega_0 L_{\rm mmc}\\ \omega_0 L_{\rm mmc} & 0\end{bmatrix}\begin{bmatrix}\Delta I_{gd}\\ \Delta I_{gq}\end{bmatrix}. \quad (26)$$

Therefore, the *dq*-axis equivalent circuit of the MMC only with the current inner loop can be obtained based on Fig. 6, as shown in Fig. 7. The PI controller of current inner loop control are equivalent as the resistor and capacitor, respectively, as shown in Fig. 7. The decoupling term and voltage feedforward are both considered, $k_{vf} = 1$ and $k_{dec} = 1$.

C. Equivalent Circuit of MMC With Current Inner Loop Control, Reactive Power Control and Virtual Admittance Control

If the reactive power control and virtual admittance control are both considered, the reference of *dq* voltage can be obtained based on (14) and expressed as

$$\begin{bmatrix}\Delta V_{gd\rm ref}\\ \Delta V_{gq\rm ref}\end{bmatrix} = -D_q\begin{bmatrix}I_{q0} & -I_{d0}\\ 0 & 0\end{bmatrix}\begin{bmatrix}\Delta V_{gd}\\ \Delta V_{gq}\end{bmatrix}$$
$$-D_q\begin{bmatrix}-U_{q0} & U_{d0}\\ 0 & 0\end{bmatrix}\begin{bmatrix}\Delta I_{gd}\\ \Delta I_{gq}\end{bmatrix}. \quad (27)$$

The reference of *dq* current can be obtained according to Fig. 6 and expressed as

$$\begin{bmatrix}\Delta I_{d\rm ref}\\ \Delta I_{q\rm ref}\end{bmatrix} = H_v(s)\begin{bmatrix}(\Delta V_{gd\rm ref}-\Delta V_{gd})\\ (\Delta V_{gd\rm ref}-\Delta V_{gq})\end{bmatrix}$$
$$+\begin{bmatrix}0 & -K_v H_v(s)\\ K_v H_v(s) & 0\end{bmatrix}\begin{bmatrix}\Delta I_{d\rm ref}\\ \Delta I_{q\rm ref}\end{bmatrix}$$

$$\Rightarrow \begin{bmatrix}\Delta I_{d\text{ref}}\\ \Delta I_{q\text{ref}}\end{bmatrix} = \begin{bmatrix}\frac{H_v(s)}{H_v^2(s)K_v^2+1} & \frac{-K_vH_v^2(s)}{H_v^2(s)K_v^2+1}\\ \frac{K_vH_v^2(s)}{H_v^2(s)K_v^2+1} & \frac{H_v(s)}{H_v^2(s)K_v^2+1}\end{bmatrix} \times \begin{bmatrix}(\Delta V_{gd\text{ref}} - \Delta V_{gd})\\ (\Delta V_{gq\text{ref}} - \Delta V_{gq})\end{bmatrix} \tag{28}$$

where K_v is the cross-decoupling term of virtual admittance control and $K_v = \omega_0 L_v$. Consequently, (29) can be obtained by substituting (28) into (26). Matrix $\boldsymbol{G_u}$ is shown in (30)

$$\begin{bmatrix}\Delta V_{gd}\\ \Delta V_{gq}\end{bmatrix} + H_I(s)\begin{bmatrix}\frac{H_v(s)}{H_v^2(s)K_v^2+1} & \frac{-K_vH_v^2(s)}{H_v^2(s)K_v^2+1}\\ \frac{K_vH_v^2(s)}{H_v^2(s)K_v^2+1} & \frac{H_v(s)}{H_v^2(s)K_v^2+1}\end{bmatrix} \times \begin{bmatrix}1+D_qI_{q0} & -D_qI_{d0}\\ 0 & 1\end{bmatrix}\begin{bmatrix}\Delta V_{gd}\\ \Delta V_{gq}\end{bmatrix} - \begin{bmatrix}k_{vf} & 0\\ 0 & k_{vf}\end{bmatrix}\begin{bmatrix}\Delta V_{gd}\\ \Delta V_{gq}\end{bmatrix} = -\boldsymbol{G_u}\begin{bmatrix}\Delta I_{gd}\\ \Delta I_{gq}\end{bmatrix} \tag{29}$$

$$\boldsymbol{G_u} = \begin{bmatrix}H_I(s)+R_{\text{mmc}}+sL_{\text{mmc}} & 0\\ 0 & H_I(s)+R_{\text{mmc}}+sL_{\text{mmc}}\end{bmatrix} + \begin{bmatrix}-\frac{H_I(s)H_v(s)D_qU_{q0}}{H_v^2(s)K_v^2+1} & \frac{H_I(s)H_v(s)D_qU_{d0}}{H_v^2(s)K_v^2+1}\\ 0 & 0\end{bmatrix} \times \begin{bmatrix}1 & -K_vH_v(s)\\ K_vH_v(s) & 1\end{bmatrix}. \tag{30}$$

For (29), matrix $[\Delta I_{gd}, \Delta I_{gq}]^T$ is divided into (31). Matrix $[\Delta I_{gId}, \Delta I_{gIq}]^T$ and $[\Delta I_{gvd}, \Delta I_{gvq}]^T$ are shown in (32) and (33)

$$\begin{bmatrix}\Delta I_{gd}\\ \Delta I_{gq}\end{bmatrix} = \begin{bmatrix}\Delta I_{gId}\\ \Delta I_{gIq}\end{bmatrix} + \begin{bmatrix}\Delta I_{gvd}\\ \Delta I_{gvq}\end{bmatrix} \tag{31}$$

$$\begin{bmatrix}\Delta I_{gId}\\ \Delta I_{gIq}\end{bmatrix} = -\boldsymbol{G_u}^{-1}\begin{bmatrix}\Delta V_{gd}\\ \Delta V_{gq}\end{bmatrix} \tag{32}$$

$$\begin{bmatrix}\Delta I_{gvd}\\ \Delta I_{gvq}\end{bmatrix} = -\boldsymbol{G_u}^{-1}\left(\frac{H_I(s)H_v(s)}{H_v^2(s)K_v^2+1} \times \begin{bmatrix}1+D_qI_{q0} & -D_qI_{d0}-K_vH_v(s)\\ K_vH_v(s)(1+D_qI_{q0}) & 1-K_vH_v(s)D_qI_{d0}\end{bmatrix} - \begin{bmatrix}k_{vf} & 0\\ 0 & k_{vf}\end{bmatrix}\right)\begin{bmatrix}\Delta V_{gd}\\ \Delta V_{gq}\end{bmatrix}. \tag{33}$$

1) Equivalent Circuit Affecting By Reactive Power Control: According to (32), (34) is obtained. K_v is beneficial for suppressing the negative resistance of sub-synchronous frequency ranges, as shown in Fig. 8

$$\begin{bmatrix}\Delta V_{gd}\\ \Delta V_{gq}\end{bmatrix} = -\begin{bmatrix}H_I(s)+R_{\text{mmc}}+sL_{\text{mmc}} & 0\\ 0 & H_I(s)+R_{\text{mmc}}+sL_{\text{mmc}}\end{bmatrix} \times \begin{bmatrix}\Delta I_{gId}\\ \Delta I_{gIq}\end{bmatrix} - \begin{bmatrix}-\frac{H_I(s)H_v(s)D_qU_{q0}}{H_v^2(s)K_v^2+1} & \frac{H_I(s)H_v(s)D_qU_{d0}}{H_v^2(s)K_v^2+1}\\ 0 & 0\end{bmatrix}\begin{bmatrix}\Delta I_{gId}\\ \Delta I_{gIq}\end{bmatrix}$$

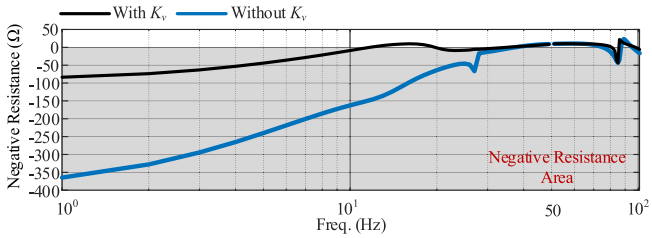

Fig. 8. Negative resistance characteristic affected by cross-coupling terms of virtual admittance control.

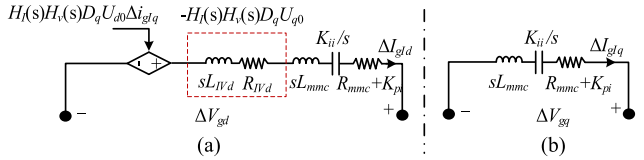

Fig. 9. Equivalent circuit with reactive power control. (a) d-axis. (b) q-axis.

$$- \begin{bmatrix}\frac{H_I(s)H_v^2(s)D_qU_{d0}K_v}{H_v^2(s)K_v^2+1} & \frac{H_I(s)H_v^2(s)D_qU_{q0}K_v}{H_v^2(s)K_v^2+1}\\ 0 & 0\end{bmatrix}\begin{bmatrix}\Delta I_{gId}\\ \Delta I_{gIq}\end{bmatrix}. \tag{34}$$

It should be noted that while the cross-coupling term K_v can improve negative resistance characteristics to some extent, however, it cannot completely eliminate negative resistance. H_v is the most fundamental origin of negative resistance. To simplify the circuit modeling and concentrate the negative resistance's main derivation, the cross-coupling term of virtual admittance control is not considered and K_v is set to 0 in the equivalent circuit's modeling process.

Therefore, the equivalent circuit of the current inner loop control considering the reactive power control and virtual admittance control can be equivalent as Fig. 9. The d-axis equivalent circuit formed by the virtual admittance control and current inner loop control is shown in Fig. 9(a) and expressed as (35). A virtual resistor and inductor can be formed in the d-axis equivalent circuit, expressed as (36). And a current-controlled voltage source can be formed in the d-axis equivalent circuit according to

$$D_qU_{q0}H_I(j\omega)H_v(j\omega) = D_qU_{q0}\frac{K_{pi}R_v - K_{ii}L_v}{L_v^2\omega^2+R_v^2} - jD_qU_{q0}\frac{K_{ii}R_v + K_{pi}L_v\omega^2}{\omega(L_v^2\omega^2+R_v^2)} \tag{35}$$

$$R_{IVd} = D_qU_{q0}\frac{-K_{pi}R_v + K_{ii}L_v}{L_v^2\omega^2+R_v^2}, L_{IVd} = D_qU_{q0}\frac{K_{ii}R_v + K_{pi}L_v\omega^2}{\omega^2(L_v^2\omega^2+R_v^2)}. \tag{36}$$

2) Equivalent Circuit Affecting by Voltage Feedforward: According to (33), (37) can be obtained. Four impedance elements

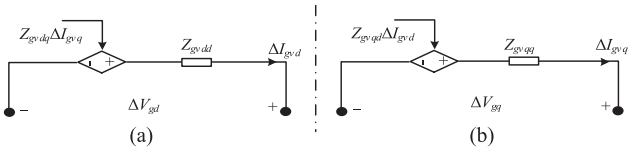

Fig. 10. Equivalent circuit without reactive power control. (a) *d*-axis. (b) *q*-axis.

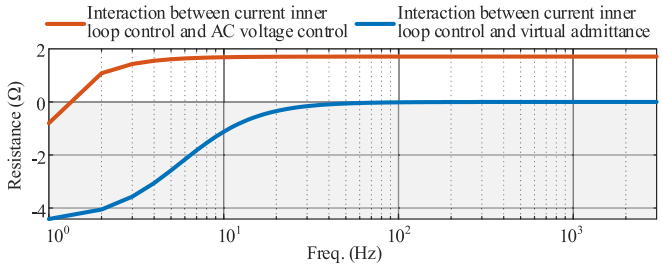

Fig. 11. Negative resistance introduced by the interaction between current inner loop and AC voltage middle loop control or virtual admittance control.

of (37) are expressed as (38)–(41). Compared to other coefficients, D_q is about 3.7818×10^{-6}, which has less effect on the impedance characteristic in (37). By considering voltage feedforward and neglecting the reactive power control, D_q is set to 0 and k_{vf} is set to 1. Z_{gdd} and Z_{gdq} are approximately equivalent as (38) and (40), respectively. Therefore, the equivalent circuit formed by the current inner loop control and virtual admittance control can be equivalent as Fig. 10. According to (38)–(41), the *dq*-axis circuit can be equivalent to virtual impedances and current-controlled voltage source, as shown in Fig. 10. It should be pointed out that the virtual impedances Z_{gvdd} and Z_{gvqq} will be further divided in to the virtual resistor, inductor and capacitor in the following section:

$$\begin{bmatrix}\Delta V_{gd}\\ \Delta V_{gq}\end{bmatrix}=\begin{bmatrix}Z_{gvdd} & Z_{gvdq}\\ Z_{gvqd} & Z_{gvqq}\end{bmatrix}\begin{bmatrix}\Delta I_{gvd}\\ \Delta I_{gvq}\end{bmatrix} \tag{37}$$

$$Z_{gvdd}=\frac{\begin{array}{c}D_qI_{d0}H_vH_I\omega_0L_{\text{mmc}}+(-D_qU_{q0}H_vH_I\\ +sL_{\text{mmc}}+H_I)(H_vH_I-k_{vf})\end{array}}{(H_vH_ID_qI_{q0}+H_vH_I-k_{vf})(H_vH_I-k_{vf})}$$

$$\approx\frac{(sL_{\text{mmc}}+H_I)}{(H_vH_I-k_{vf})} \tag{38}$$

$$Z_{gvqq}=\frac{sL_{\text{mmc}}+H_I}{H_vH_I-k_{vf}} \tag{39}$$

$$Z_{gvdq}=\frac{\begin{array}{c}H_vH_ID_qI_{d0}(sL_{\text{mmc}}+H_I)+(D_qU_{d0}H_vH_I\\ -\omega_0L_{\text{mmc}})(H_vH_I-k_{vf})\end{array}}{(H_vH_ID_qI_{q0}+H_vH_I-k_{vf})(H_vH_I-k_{vf})}$$

$$\approx\frac{(-\omega_0L_{\text{mmc}})}{(H_vH_I-k_{vf})} \tag{40}$$

$$Z_{gvqd}=\frac{\omega_0L_{\text{mmc}}}{H_vH_I-k_{vf}}. \tag{41}$$

IV. Small-Signal Instability Mechanism Analysis

A. Negative Resistance Introduced By Reactive Power Outer Loop, Virtual Admittance Control and Current Inner Loop

According to the established equivalent circuit model, if the reactive power outer loop and virtual admittance control are not considered, the current inner loop is a linear link and there is no negative resistance, as shown in (34) and Fig. 7. If these elements are both considered, according to (35), the reactive power outer loop and virtual admittance control introduce the negative resistance into the *d*-axis equivalent circuit of the current inner loop, as shown in Fig. 11.

TABLE I
Parameters of the MMC

	Parameter	Value
Electrical System	Rated active power	1100 MW
	Rated AC-side voltage	416 kV
	Rated DC-side voltage	±400 kV
	Submodules in each arm	400
	Submodule capacitance	11 mF
	Arm inductance	133 mH
	Ratio of transformer	525 / 416
	Leakage reactance of transformer	61.73 mH
Control System	Active power controller (D_p)	2.8280×10^{-9}
	Reactive power controller (D_q)	3.7818×10^{-6}
	Inner-loop PI controller (k_{pi}, k_{ii})	57, 5000
	CCSC PI controller (k_{pc}, k_{ic})	79.007, 3823.4
	Virtual admittance control (R_v, L_v)/p.u.	0.1, 0.3
	R_{LP}, T_{LP}	1.0, 0.1
	R_{qd}, T_{qd}	4.0, 0.1
	Control delay (T_d)	200 μs

The controller parameters used for negative resistance analysis in Fig. 11 are given in Table I. The proportional and integral coefficients for the ac voltage middle loop control are set to 0.03 and 0.09, respectively. If the ac voltage middle loop control is used to substitute the virtual admittance control, which means the PI controller is adopted, expressed as (42). $R_{\text{AC}}(\omega)$ is the real part of transfer function $H_I(j\omega)\cdot H_{\text{ac}}(j\omega)$. The negative resistance can be suppressed if the AC voltage middle loop control is used, as shown in Fig. 11. Therefore, the negative resistance is mainly introduced by the virtual admittance control

$$R_{\text{AC}}(\omega)=\text{Real}\left[H_I(j\omega)H_{\text{ac}}(j\omega)\right]=K_{pac}K_{pi}-\frac{K_{ii}K_{iac}}{\omega^2}. \tag{42}$$

1) Negative Resistance in Non-Diagonal Impedance Element Z_{dq}*:* In Fig. 9, $D_q\cdot U_{q0}\cdot H_I(s)\cdot H_v(s)$ will introduce the negative resistance in the nondiagonal impedance element Z_{dq}. For the negative resistance introduced by the virtual admittance control and current inner loop of (43), the negative resistance dominated by the R_v and L_v is shown in Fig. 12.

It should point out that the accurate design of R_v and L_v must involve a tradeoff among small-signal stability, fault current limiting [4], [21], and power transmission limitation [38]. However, to study the negative resistance introduced by virtual admittance control, the virtual resistance is set within a wider range of 0 to 0.3 p.u., while the virtual inductance is configured within a wider

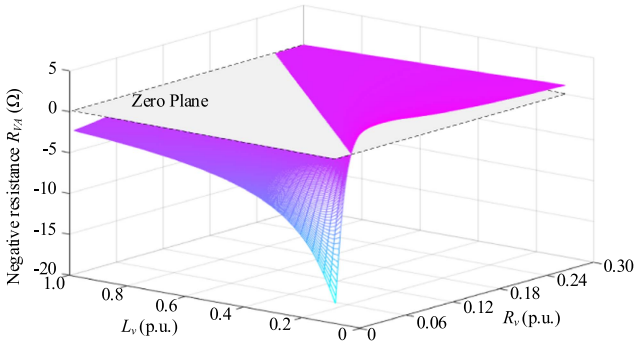

Fig. 12. Negative resistance R_{VA} dominated by the virtual admittance control in (43).

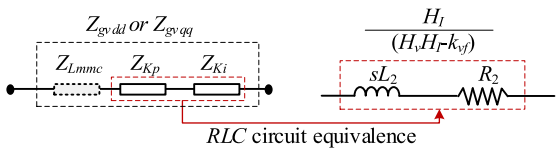

Fig. 13. Equivalent circuit of the resistor R_1 and capacitor C_1.

range of 0 to 1.0 p.u. In (43), $R_{\mathrm{VA}}(\omega)$ is the real part of transfer function $H_I(j\omega)\cdot H_v(j\omega)$

$$R_{\mathrm{VA}}(\omega) = \mathrm{Real}\left[H_I(j\omega)\,H_v(j\omega)\right] = \frac{K_{pi}R_v - K_{ii}L_v}{L_v^2\omega^2 + R_v^2}. \tag{43}$$

As shown in Fig. 12, increasing R_v can help to alleviate the negative resistance characteristic. The impact of L_v on negative resistance is influenced by the magnitude of R_v. When R_v is less, increasing L_v can help to alleviate negative resistance. When R_v is larger, increasing L_v exacerbates the negative resistance. Overall, the negative resistance can be suppressed with increasing the R_v.

2) Negative Resistance in Diagonal Impedance Element Z_{dd} *and* Z_{qq}*:* According to (38)–(39) and (40)–(41), compared with the diagonal impedance elements Z_{gvdd} and Z_{gvqq}, the negative resistances introduced by the non-diagonal elements Z_{gvdq} and Z_{gvqd} are rather less, which can be neglected in this section. In (37), the negative resistances of the diagonal impedance elements Z_{gvdd} and Z_{gvqq} in (38) and (39) are mainly introduced by the interaction between the current inner loop control, virtual admittance control, and voltage feedforward. The virtual impedance elements Z_{gvdd} or Z_{gvqq} can be divided into three parts including $Z_{Kp}(s)$, $Z_{Ki}(s)$, and $Z_{Lmmc}(s)$, expressed as (44). Their equivalent circuits are shown in Fig. 13

$$\begin{aligned} &Z_{gvdd}(s) = Z_{gvqq}(s) = Z_{Kp}(s) + Z_{L\mathrm{mmc}}(s) + Z_{Ki}(s). \\ &\Rightarrow Z_{Kp}(s) = \frac{K_{pi}}{H_vH_I - k_{vf}},\ Z_{L\mathrm{mmc}}(s) \\ &= \frac{sL_{\mathrm{mmc}}}{H_vH_I - k_{vf}}, Z_{Ki}(s) = \frac{K_{ii}}{s(H_vH_I - k_{vf})} \end{aligned} \tag{44}$$

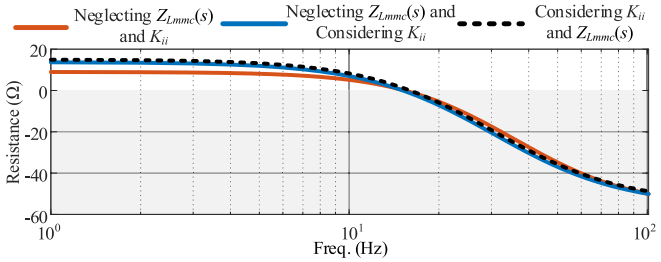

Fig. 14. Resistive characteristic affected by the interaction between current inner loop control, virtual admittance control and voltage feedforward.

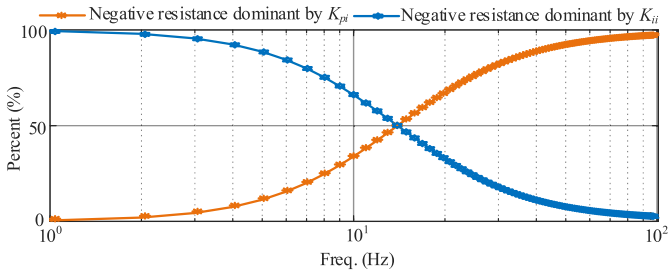

Fig. 15. Negative resistance percent dominated by K_{pi} and K_{ii}.

Fig. 14 is resistance curve for the real part of Z_{gvdd} or Z_{gvqq}. In (44), the inductive component $Z_{L\mathrm{mmc}}(s)$ will not largely affect the negative resistance which can be neglected in this section, as shown in the black dashed and blue curves in Fig. 14. Therefore, the negative resistance of Z_{gvdd} or Z_{gvqq} are dominated by $Z_{Kp}(s)$ and $Z_{Ki}(s)$ of (44), which can be expressed as

$$Z_{Kp}(s) + Z_{Ki}(s) = \frac{H_I}{H_vH_I - k_{vf}} = \frac{K_{pi} + K_{ii}/s}{\frac{K_{pi}+K_{ii}/s}{R_v+sL_v} - k_{vf}}. \tag{45}$$

In (45), negative resistance percent dominated by K_{pi} and K_{ii} is expressed as (46), where R_{INne} represents the real part of $Z_{Kp}(s)+Z_{Ki}(s)$, ΔK_{pi} and ΔK_{ii} represent the variation of the PI parameters of current inner loop control, $\Delta R_{INne}(\Delta K_{pi})$ and $\Delta R_{INne}(\Delta K_{ii})$ represent the variation of the negative resistance dominated by ΔK_{pi} and ΔK_{ii}, respectively,

$$\begin{aligned} \mathrm{per}_{K_{pi}}(\omega) &= \frac{\frac{\Delta K_{pi}}{\Delta R_{INne}(\Delta K_{pi})}}{\frac{\Delta K_{pi}}{\Delta R_{INne}(\Delta K_{pi})} + \frac{\Delta K_{ii}}{\Delta R_{INne}(\Delta K_{ii})}} \times 100 \\ \mathrm{per}_{K_{ii}}(\omega) &= \frac{\frac{\Delta K_{ii}}{\Delta R_{INne}(\Delta K_{pi})}}{\frac{\Delta K_{pi}}{\Delta R_{INne}(\Delta K_{pi})} + \frac{\Delta K_{ii}}{\Delta R_{INne}(\Delta K_{ii})}} \times 100. \end{aligned} \tag{46}$$

According to (46), the negative resistance percent is shown as Fig. 15. Combined with the negative resistance curves of Figs. 14 and 15, it is apparent that the negative resistance is largely dominated by K_{pi}. The K_{ii} can be neglected when analyzing the negative resistance. Thus, the $Z_{Kp}(s)$ and $Z_{Ki}(s)$ are simplified as (47). Equivalent circuit of Z_{gvdd} or Z_{gvqq} in Fig. 10 can be simplified as Fig. 13. The virtual resistance R_2 and virtual inductance L_2 of Fig. 13 are expressed in (48) and (49). Due to the low-pass characteristic of the virtual admittance control, the

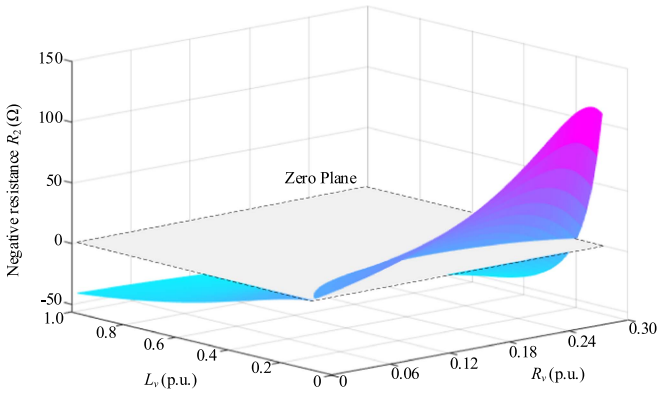

Fig. 16. Negative resistance dominated by R_v and L_v in R_2.

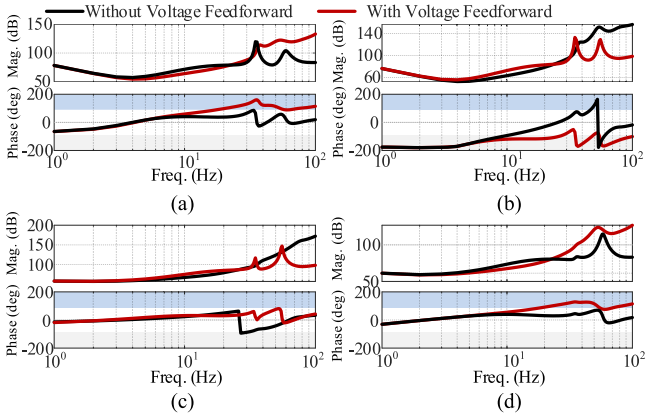

Fig. 17. dq domain impedance of GFM-based MMC. (a) Z_{dd}. (b) Z_{dq}. (c) Z_{qd}. (d) Z_{qq}.

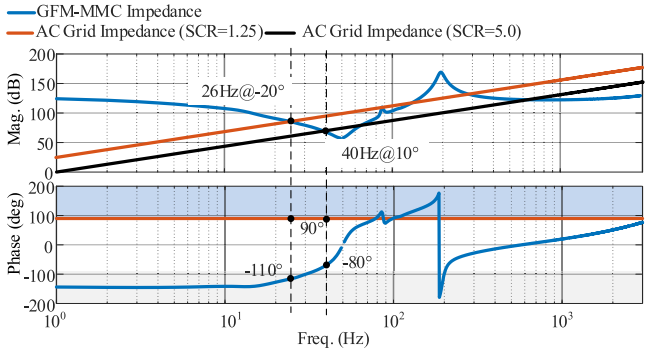

Fig. 18. Instable analysis of GFM-based MMC under the weak grid conditions.

combined effect of voltage feedforward and K_{pi} would introduce a negative resistance in R_2 within the frequency ranges which are beyond the cut-off frequency of the virtual admittance control

$$\frac{H_I}{H_v H_I - k_{vf}} \approx \frac{1}{\frac{1}{R_v + sL_v} - \frac{k_{vf}}{K_{pi}}} = R_2 + sL_2 \tag{47}$$

$$R_2 = \frac{\frac{R_v}{L_v^2\omega^2 + R_v^2} - \frac{k_{vf}}{K_{pi}}}{\left(\frac{R_v}{L_v^2\omega^2 + R_v^2} - \frac{k_{vf}}{K_{pi}}\right)^2 + \frac{L_v^2\omega^2}{(L_v^2\omega^2 + R_v^2)^2}} \tag{48}$$

$$L_2 = \frac{\frac{L_v}{L_v^2\omega^2 + R_v^2}}{\left(\frac{R_v}{L_v^2\omega^2 + R_v^2} - \frac{k_{vf}}{K_{pi}}\right)^2 + \frac{L_v^2\omega^2}{(L_v^2\omega^2 + R_v^2)^2}}. \tag{49}$$

As shown in Fig. 16, the negative resistance R_2 is exacerbated with increasing the L_v. The negative resistance R_2 can be alleviated with increasing the R_v when L_v is small. However, the virtual resistance R_v cannot be infinitely increased because its suppression effect on negative resistance exhibits non monotonic characteristics, as shown in Fig. 16.

B. Instable Mechanism of GFM-MMC

According to the equivalent circuit of GFM-MMC, the dq domain impedances of GFM-based MMC are shown in Fig. 17. On the basis of the negative resistance's analysis, if the voltage feedforward is considered, the inductive negative resistance exists in the diagonal impedance. The capacitive negative resistance exists in the nondiagonal impedance. If the voltage feedforward is not considered, the negative resistance can be largely alleviated.

Based on impedance transformation of (50), the impedance under dq domain can be transformed into the modified sequence-domaisn [39]. After frequency offset, the positive-sequence impedance of the GFM-based MMC is shown in (51). After the coordinate transformation, the negative resistance of the dq domain leads to capacitive negative resistance in the low-frequency range of the sequence impedance, as shown in Fig. 18. Due to the dominant inductive characteristics of HVDC transmission lines, when the equivalent grid strength decreases to 1.25, they intersect with GFM-based MMC in the negative resistance range, making it prone to oscillatory instability, as shown in Fig. 18

$$\begin{bmatrix} Z_{dd\pm} & Z_{dq\pm} \\ Z_{qd\pm} & Z_{qq\pm} \end{bmatrix} = A_Z \begin{bmatrix} Z_{dd} & Z_{dq} \\ Z_{qd} & Z_{qq} \end{bmatrix} A_Z^{-1} = \begin{bmatrix} -R_{dd\pm} + jX_{dd\pm} & -R_{dq\pm} - jX_{dq\pm} \\ R_{qd\pm} + jX_{qd\pm} & -R_{qq\pm} + jX_{qq\pm} \end{bmatrix} \tag{50}$$

$$\begin{aligned} Z(|f \pm 50|) &= -R_{dd\pm} + jX_{dd\pm} - \frac{-R_{dq\pm} - jX_{dq\pm}}{-R_{qq\pm} + jX_{qq\pm}} \\ &= -R_{dd\pm} - \frac{R_{qq\pm}R_{dq\pm} - X_{dq\pm}X_{qq\pm}}{R_{qq\pm}^2 + X_{qq\pm}^2} \\ &\quad + j\left(X_{dd\pm} - \frac{X_{dq\pm}R_{qq\pm} + X_{qq\pm}R_{dq\pm}}{R_{qq\pm}^2 + X_{qq\pm}^2}\right). \end{aligned} \tag{51}$$

V. Small-Signal Stability Enhancement Method

A. Design of Small-Signal Stability Enhancement Method

The design of R_v and L_v involves a trade-off among multi-objective. A systematic approach should consider the worst-case grid condition (e.g., low SCR), ensure the fault current remains within device limits, and maintain the desired power transmission capacity. However, as shown in Figs. 12 and 16, due to the

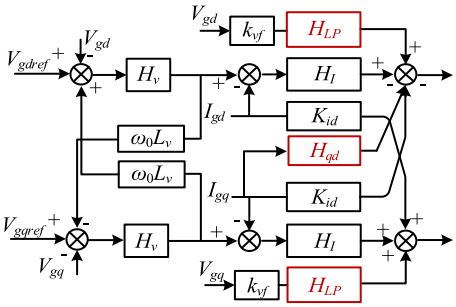

Fig. 19. Small-signal stability enhancing method.

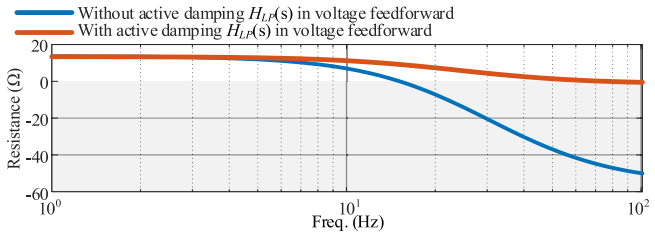

Fig. 20. Resistive characteristic affected by active damping H_{LP}(s) in voltage feedforward.

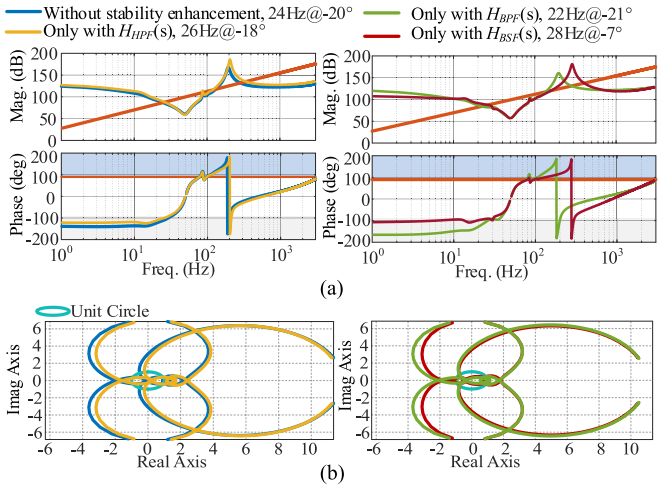

Fig. 21. Small-signal stability enhancing diagram. (a) Bode diagram. (b) Nyquist diagram.

nonmonotonic influence of R_v and L_v on negative resistance, parameter tuning alone may be insufficient to guarantee stability, necessitating additional active damping measures. Therefore, an additional structure is proposed in this section to suppress the negative resistance.

1) Cross-Coupled Active Damping of Current Inner Loop: Based on the analysis of negative resistance presented in Section IV, under the influence of reactive power control, the interaction between virtual admittance control and current inner loop control introduces negative resistance in the upper-right element of the impedances of the GFM-based MMC. Therefore, a cross-coupled active damping control H_{qd} is incorporated into the d-axis voltage feedforward path via the q-axis current, as illustrated in Fig. 19. The structure and parameters of H_{qd} are designed according to (52) to mitigate the negative resistance in the upper-right impedance element of (34)

$$H_{qd} = \frac{R_{vqd} + sL_{vqd}}{s^2 + s\omega_{qd}} = D_q U_{d0} \left(K_{pi} + \frac{K_{ii}}{s} \right) \frac{1}{R_v + sL_v}$$
$$\Rightarrow R_{vqd} = \frac{D_q U_{d0} \omega_{qd} K_{ii}}{R_v},$$
$$L_{vqd} = \frac{D_q U_{d0} \omega_{qd} K_{pi}}{R_v}, \omega_{qd} = \frac{R_v}{L_v}. \tag{52}$$

2) Active Damping in Voltage Feedforward: As shown in (47) and Fig. 17, the introduction of negative resistance is critically dependent on voltage feedforward, as analyzed in Section IV. If voltage feedforward is not considered, the negative resistance resulting from the low-pass filtering characteristic of virtual admittance control in the impedance diagonal elements will be eliminated. Therefore, it is proposed to add active damping in the voltage feedforward to eliminate the effect of negative resistance. As analyzed in (47), the low-pass filter H_{LP}(s) is required to form the active damping within the voltage feedforward to eliminate the negative resistance, expressed as (53) and shown in Fig. 19. The cut-off frequency ω_{LP} and the proportional coefficient K_{LP} of H_{LP}(s) are designed based on the equivalent cut-off frequency and amplitude of virtual admittance control, expressed as (53). As shown in Fig. 20, the adoption of low-pass filter H_{LP}(s) can suppress the negative resistance, based on the analysis of Fig. 14

$$\frac{1}{\frac{1}{R_v + sL_v} - \frac{k_{vf}}{K_{pi}} H_{LP}(s)} \Rightarrow H_{LP}(s) = K_{LP} \frac{\omega_{LP}}{(\omega_{LP} + s)}$$
$$\omega_{LP} = \frac{R_v}{L_v}, \; K_{LP} = k_{vf} \frac{K_{pi}}{R_v}. \tag{53}$$

B. Comparing With the Existing Method

The stability analysis results of bode diagram and Nyquist diagram are shown as Fig. 21. If the traditional active damping methods, such as band rejection filters [35], high pass filters [36], and band pass filters [37] are adopted in the current inner loop control, the small-signal stability margin is rarely improved. As shown in Fig. 22, small-signal stability can be improved to some degree if the H_{qd}(s) and H_{LP}(s) are adopted, respectively. If they are both adopted, the stability is further improved.

VI. Simulation and Experimental Results

The simulation model of GFM-based MMC with virtual admittance control is established in MATLAB/Simulink according to the topology and control structure in Figs. 1 and 2. The parameters of MMC are given in Table I.

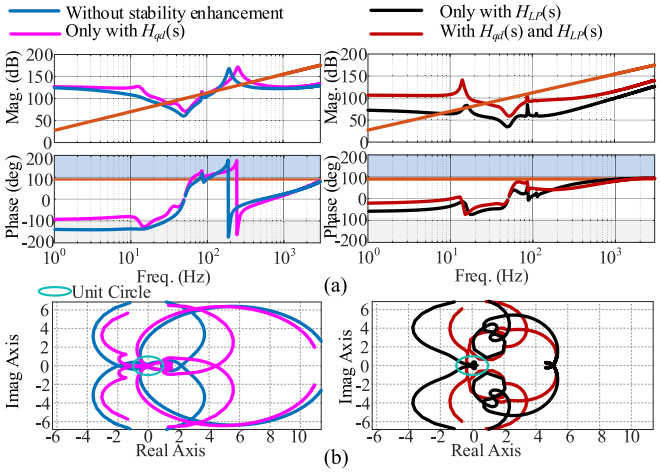

Fig. 22. Small-signal stability enhancing diagram. (a) Bode diagram. (b) Nyquist diagram.

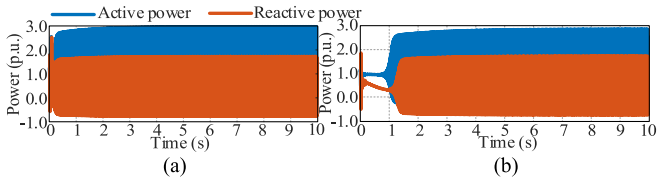

Fig. 23. Simulation verification. (a) Without stability enhancement. (b) Only with H_{BSF}.

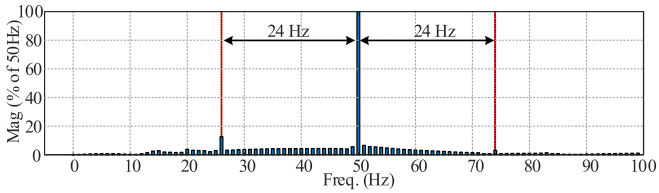

Fig. 24. Oscillation frequency under the three-phase coordinate system.

A. Simulation Verification of the Small-Signal Stability Enhancement

Under ultra-weak grid condition with SCR of 1.25, oscillations emerge when considering voltage feedforward and virtual admittance control without using any enhancement strategy, as shown in Fig. 23(a). The oscillation frequency of active and reactive power is 24 Hz, corresponding to 26/74 Hz in the three-phase coordinate system, as shown in Fig. 24. When traditional active damping methods [35], [36], [37] are used, oscillations persist and stability remains unimproved, as demonstrated by the power waveforms in Fig. 23(b).

When cross-coupled active damping H_{qd}(s) is adopted, small-signal stability improves to some extent. However, oscillations reappear after $t = 3.5$ s, as shown in Fig. 25(a). With the use of active damping H_{LP}(s) for voltage feedforward, small-signal stability is enhanced, and the power waveforms exhibit a damped response, as depicted in Fig. 25(b). If both cross-coupled active damping H_{qd}(s) and active damping H_{LP}(s) are used, the oscillations in active and reactive power are effectively suppressed, as shown in Fig. 25(c).

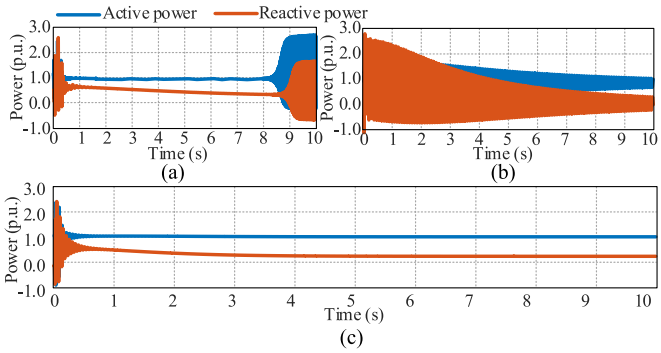

Fig. 25. Simulation verification of the proposed method. (a) Only with H_{qd}(s). (b) Only with H_{LP}(s). (c) With H_{qd}(s) and H_{LP}(s).

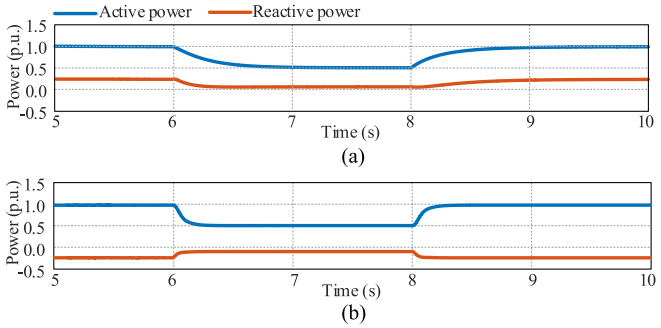

Fig. 26. Verification of the dynamic response capability if the proposed method is adopted. (a) Weak grid with SCR of 1.25. (b) Strong grid with SCR of 10.0.

B. Simulation Verification of the Dynamic Response Capability

When the proposed $H_{qd}(s)$ and $H_{LP}(s)$ are implemented with the virtual admittance control parameters given in Table I, the system remains stable and accurately track the power reference changing from 1.0 to 0.5 p.u., as shown in Fig. 26. According to Fig. 26, the proposed control method is demonstrated to ensure stable system operation while maintaining satisfactory dynamic performance under both extremely weak and strong grid conditions.

The theoretical analysis reveals that system stability cannot be maintained with $H_{qd}(s)$ alone under extremely weak grids of SCR $= 1.25$. To highlight the superior dynamic performance of the proposed method, the simulation results in Fig. 27 with SCR of 3.0 demonstrate that the system exhibits oscillatory behavior during power reference step changes if only the $H_{qd}(s)$ is adopted. In contrast, the power oscillations can be effectively suppressed if both $H_{qd}(s)$ and H_{LP}(s) are simultaneously adopted, enabling accurate tracking of power reference variations.

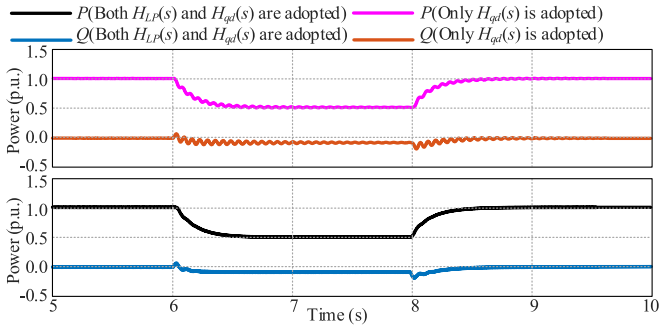

Fig. 27. Verification of the dynamic response capability of the proposed method under the weak grid with SCR of 3.0.

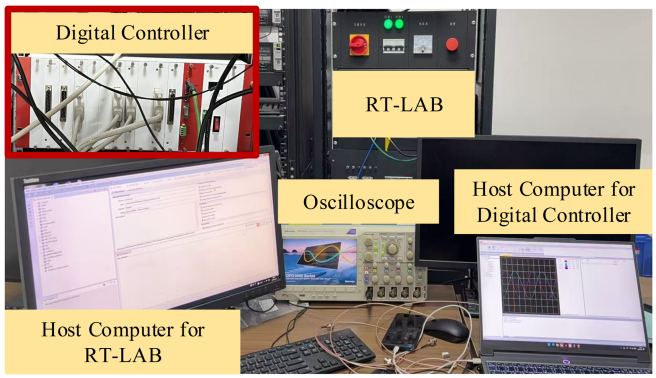

Fig. 28. HIL experimental platform.

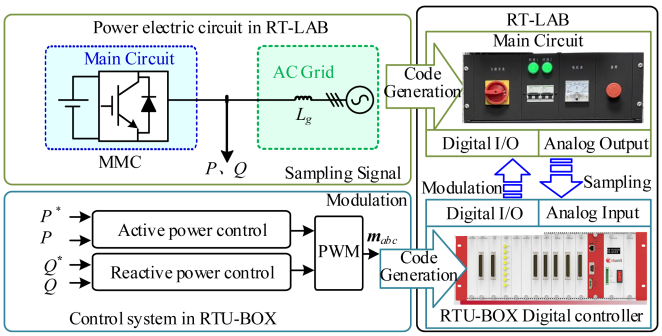

Fig. 29. Implementation of HIL experiment platform for an MMC system.

C. Experimental Verification

Real-time controller hardware-in-the-loop (HIL) experiments were conducted to further validate the effectiveness of the proposed method. A photograph of the HIL experimental platform is provided Fig. 28. The digital controller is built around a TMS320C28346 digital signal processor and a field-programmable gate array (FPGA). The system's circuit components are modeled in RT-LAB, while the MMC control algorithm is executed on the digital controller.

As depicted in Fig. 29, the main circuit is imported from the host PC into the FPGA of the real-time simulator chassis via RT-LAB. The FPGA operates in a closed-loop configuration with the digital controller (RTU-BOX) through a connection

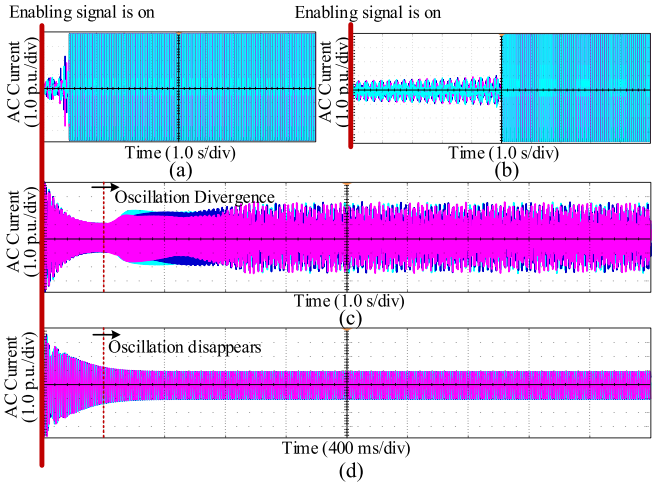

Fig. 30. Experimental verification of the small-signal stability enhancement. (a) Without stability enhancement. (b) Only with H_{BSF}. (c) Only with H_{qd}(s). (d) With H_{qd}(s) and H_{LP}(s).

box, and the output waveforms are displayed on an oscilloscope. The RTU-BOX samples current and voltage signals from the main circuit and feeds the digital control signals back to the power circuit in RT-LAB, ensuring a closed-loop system. The experimental model initiates operation when the enabling signal is activated. The experimental parameters for the MMC are given in Table I.

Under ultra-weak grid conditions with an SCR of 1.25, the system becomes unstable without any small-signal stability enhancement strategy, as evidenced by the ac current waveform in Fig. 30(a). When only the active damping H_{BSF} is applied, oscillations persist, and small-signal stability remains unimproved, as shown in Fig. 30(b). With the implementation of cross-coupled active damping H_{qd}(s), small-signal stability improves to some extent, but oscillations still remain and diverge, as illustrated in Fig. 30(c). When both cross-coupled active damping H_{qd}(s) and active damping H_{LP}(s) for voltage feedforward are employed, oscillations are effectively suppressed, as demonstrated in Fig. 30(d).

VII. Conclusion

The small-signal stability of GFM-based MMC is normally considered to be enhanced under weak grid conditions. Virtual admittance control is typically employed to enhance overcurrent suppression capabilities. However, the proposed equivalent circuit model reveals that the interaction between the virtual admittance control and the current inner loop introduces negative resistance into the d-axis and q-axis circuits, potentially compromising the small-signal stability enhancement of GFM-based MMC under weak grid conditions. The primary conclusions derived from this article are as follows

1) Low-pass characteristics are exhibited by the virtual admittance control. Negative resistance emerges in frequency ranges exceeding the cutoff frequency of the virtual admittance control, influenced by voltage feedforward and the proportional coefficients of the current inner loop.

This imparts "inductive negative resistance" characteristics to the *dq* axis equivalent circuit of the GFM-based MMC.

2) Under the influence of reactive power control, the interaction between the virtual admittance control and the current inner loop leads to the emergence of "capacitive negative resistance" in the *q*-axis current-controlled voltage sources of the equivalent circuit, which corresponds to the upper-right element of the GFM-MMC impedance matrix.
3) After coordinate transformation and frequency offset, "capacitive negative resistance" emerges in the low-frequency range of the sequence impedance for GFM-based MMC. Small-signal instability is prone to arise as the inductive characteristic of transmission lines intensifies and the SCR decreases.
4) A stabilization approach for enhancing the small-signal stability of GFM-based MMC with virtual admittance control was proposed, which incorporates low-pass filters into the voltage feedforward path and another active damping into the cross-coupled path of the current inner loop control. By reasonably designing the parameters of the active damping, the negative resistance introduced by virtual admittance control is limited, thereby enhancing the stability of GFM-based MMC.

REFERENCES

[1] M. A. Perez, S. Bernet, J. Rodriguez, S. Kouro, and R. Lizana, "Circuit topologies, modelling, control schemes, and applications of modular multilevel converters," *IEEE Trans. Power Electron*, vol. 30, no. 1, pp. 4–17, Jan. 2015.

[2] J. Lyu, J. Yin, and L. Gao, "Analysis and control of multi-mode oscillations in multi-infeed MMC-HVDC systems," *IEEE Trans. Power Del.*, vol. 40, no. 2, pp. 1203–1213, Apr. 2025, early access.

[3] D. Pattabiraman, R. H. Lasseter, and T. M. Jahns, "Comparison of grid following and grid forming control for a high inverter penetration power system," in *Proc. IEEE Power Energy Soc. Gen. Meeting*, 2018, pp. 1–5.

[4] Q. Taoufik, H. Wu, X. Wang, and I. Colak, "Variable virtual impedance based overcurrent protection for grid-forming inverters: Small-signal, large-signal analysis and improvement," *IEEE Trans. Smart Grid*, vol. 14, no. 5, pp. 3324–3336, Sep. 2023.

[5] X. Wang, M. G. Taul, H. Wu, Y. Liao, F. Blaabjerg, and L. Harnefors, "Grid-synchronization stability of converter-based resources—An overview," *IEEE Open J. Ind. Appl.*, vol. 1, pp. 115–134, Aug. 2020.

[6] R. Rosso, X. Wang, M. Liserre, X. Lu, and S. Engelken, "Grid-forming converters: Control approaches, grid-synchronization, and future trends–A review," *IEEE Open J. Ind. Appl.*, vol. 2, pp. 93–109, 2021.

[7] Y. Li, Y. Gu, and T. C. Green, "Revisiting grid-forming and grid-following inverters: A duality theory," *IEEE Trans. Power Syst.*, vol. 37, no. 6, pp. 4541–4554, Nov. 2022.

[8] M. Yang, X. Wang, W. Sima, T. Yuan, P. Sun, and H. Liu, "Air-core transformer-based solid-state fault-current limiter for bidirectional HVDC systems," *IEEE Trans. Ind. Electron.*, vol. 69, no. 5, pp. 4914–4925, May 2022.

[9] G.-W. Kim and H.-S. Choi, "Applicability analysis of a multi-filar meander R-SFCL and an RSC-DCCB in an MMC-MTDC grid," *IEEE Trans. Appl. Supercond.*, vol. 33, no. 5, Aug. 2023, Art. no. 5600507.

[10] N. Hesam, S. Mehran, B. Ebrahim, and A. Mehdi, "A new structure of fault current limiter based on the system impedance with fast eliminating method and simple control procedure," *IEEE Trans. Ind. Electron.*, vol. 65, no. 1, pp. 261–269, Jan. 2018.

[11] Y. Zhang, Y. Xu, and M. Saeedifard, "Model-based design for reactors of the modular multilevel converter," *IEEE Trans Power Electron*, vol. 38, no. 6, pp. 6863–6873, Jun. 2023.

[12] J. Cui, C. Jia, L. Qu, and W. Qiao, "A tunable-inductor-based fault current limiter," *IEEE Trans. Ind. Appl.*, vol. 61, no. 3, pp. 4992–5002, May/Jun. 2025, doi: 10.1109/TIA.2025.3540730.

[13] L. Huang, H. Xin, Z. Wang, L. Zhang, K. Wu, and J. Hu, "Transient stability analysis and control design of droop-controlled voltage source converters considering current limitation," *IEEE Trans. Smart Grid*, vol. 10, no. 1, pp. 578–591, Jan. 2019.

[14] B. Fan and X. Wang, "Fault recovery analysis of grid-forming inverters with priority-based current limiters," *IEEE Trans. Power Syst.*, vol. 38, no. 6, pp. 5102–5112, Nov. 2023.

[15] M. G. Taul, X. Wang, P. Davari, and F. Blaabjerg, "Current limiting control with enhanced dynamics of grid-forming converters during fault conditions," *IEEE J. Emerg. Sel. Topics Power Electron.*, vol. 8, no. 2, pp. 1062–1073, Jun. 2020.

[16] E. Rokrok, T. Qoria, A. Bruyere, B. Francois, and X. Guillaud, "Transient stability assessment and enhancement of grid-forming converters embedding current reference saturation as current limiting strategy," *IEEE Trans. Power Syst.*, vol. 37, no. 2, pp. 1519–1531, Mar. 2022.

[17] J. Freytes, J. Li, G. de Préville, and M. Thouvenin, "Grid-forming control with current limitation for MMC under unbalanced fault ride-through," *IEEE Trans. Power Del.*, vol. 36, no. 3, pp. 1914–1916, Jun. 2021.

[18] A. D. Paquette and D. M. Divan, "Virtual impedance current limiting for inverters in microgrids with synchronous generators," *IEEE Trans. Ind. Appl.*, vol. 51, no. 2, pp. 1630–1638, Mar./Apr. 2015.

[19] X. Wang, Y. W. Li, F. Blaabjerg, and P. C. Loh, "Virtual-impedance based control for voltage-source and current-source converters," *IEEE Trans. Power Electron.*, vol. 30, no. 12, pp. 7019–7037, Dec. 2015.

[20] H. Wu and X. Wang, "Small-signal modeling and controller parameters tuning of grid-forming VSCs with adaptive virtual impedance based current limitation," *IEEE Trans. Power Electron.*, vol. 37, no. 6, pp. 7185–7199, Jun. 2022.

[21] B. Fan, T. Liu, F. Zhao, H. Wu, and X. Wang, "A review of current-limiting control of grid-forming inverters under symmetrical disturbances," *IEEE Open J. Power Electron.*, vol. 3, pp. 955–969, Dec. 2022.

[22] Y. Sun, D. Kong, Z. Zhang, Y. Wang, H. He, and M. L. Heldwein, "Decoupled distributed control of offshore wind farms connected to DR-HVDC based on novel adaptive virtual impedance," *IEEE Trans. Power Electron.*, vol. 39, no. 11, pp. 15242–15256, Nov. 2024.

[23] Z. Gong, C. Liu, Y. Gui, F. F. da Silva, and C. L. Bak, "Power decoupling method for voltage source inverters using grid voltage modulated direct Power control in unbalanced system," *IEEE Trans. Power Electron.*, vol. 38, no. 3, pp. 3084–3099, Mar. 2023.

[24] D. Li et al., "A negative sequence impedance design and regulation strategy for negative sequence current sharing among grid-forming sources in microgrids considering topology impacts," *IEEE Open J. Power Electron*, vol. 5, pp. 402–413, Mar. 2024.

[25] A. Das, A. Shukla, A. B. Shyam, S. Anand, J. M. Guerreo, and S. R. Sahoo, "A distributed-controlled harmonic virtual impedance loop for AC microgrids," *IEEE Trans. Ind. Electron.*, vol. 68, no. 5, pp. 3949–3961, May 2021.

[26] R. Pan, G. Tang, S. Liu, and Z. He, "Impedance analysis of grid forming control based modular multilevel converters," *J. Modern Power Syst. Clean Energy*, vol. 11, no. 3, pp. 967–979, May 2023.

[27] L. Huang, H. Xin, and Z. Wang, "Damping low-frequency oscillations through VSC-HVDC stations operated as virtual synchronous machines," *IEEE Trans. Power Electron.*, vol. 34, no. 6, pp. 5803–5818, Jun. 2019.

[28] H. Zhang et al., "Grid forming converters in renewable energy sources dominated power grid: Control strategy, stability, application, and challenges," *J. Modern Power Syst. Clean Energy*, vol. 9, no. 6, pp. 1239–1256, Nov. 2021.

[29] C. Guo, L. Xu, S. Yang, and W. Jiang, "A supplementary damping control for MMC-HVDC system to mitigate the low-frequency oscillation under low inertia condition," *IEEE Trans. Power Del.*, vol. 38, no. 1, pp. 287–298, Feb. 2023.

[30] M. Nahalparvari, M. Asoodar, S. Norrga, and H.-P. Nee, "AC-side impedance-based stability assessment in grid-forming modular multilevel converters," *IEEE Access*, vol. 12, pp. 23514–23528, Feb. 2024.

[31] J. Lyu, X. Zhang, X. Cai, and M. Molinas, "Harmonic state-space based small-signal impedance modeling of a modular multilevel converter with consideration of internal harmonic dynamics," *IEEE Trans. Power Electron.*, vol. 34, no. 3, pp. 2134–2148, Mar. 2019.

[32] J. Lyu, J. Yin, H. Zhu, and X. Cai, "Impedance modeling and stability analysis of energy controlled modular multilevel converter," *IEEE Trans. Power Del.*, vol. 38, no. 3, pp. 1868–1881, Jun. 2023.

[33] Y. Li, Y. Gu, Y. Zhu, A. Junyent-Ferré, X. Xiang, and T. C. Green, "Impedance circuit model of grid-forming inverter: Visualizing control algorithms as circuit elements," *IEEE Trans. Power Electron.*, vol. 36, no. 3, pp. 3377–3395, Mar. 2021.

[34] L. Gao, J. Lyu, X. Zong, H. Wang, and X. Cai, "Reactive power hybrid synchronization control for oscillatory stability enhancement of grid-connected inverters under ultraweak grids," *IEEE Trans. Power Electron*, vol. 40, no. 11, pp. 16837–16852, Nov. 2025.
[35] H. Liu, X. Xie, Y. Li, H. Liu, and Y. Hu, "Mitigation of SSR by embedding subsynchronous notch filters into DFIG converter controllers," *IET Gener. Transmiss. Distrib.*, vol. 11, no. 11, pp. 2888–2896, Sep. 2017.
[36] Y. Li et al., "Modeling and damping control of modular multilevel converter based DC grid," *IEEE Trans. Power Syst.*, vol. 33, no. 1, pp. 723–735, Jan. 2018.
[37] Y. Rao, J. Lyu, Y. Wang, and X. Cai, "Adaptive mitigation control for wideband oscillations of offshore wind farms with MMC-HVDC system," *CSEE J Power Energy Syst*, vol. 11, no. 1, pp. 208–216, Jan. 2025.
[38] L. Zhan, B. Hu, L. Chen, Y. Liao, M. Li, and H. Nian, "Transient stability enhancement of current limited-GFM inverters based on varying virtual impedance," *IEEE Trans. Ind. Electron*, vol. 71, no. 12, pp. 15946–15958, Dec. 2024.
[39] A. Rygg, M. Molinas, C. Zhang, and X. Cai, "A modified sequence-domain impedance definition and its equivalence to the dq-domain impedance definition for the stability analysis of AC power electronic systems," *IEEE J. Emerg. Select. Topics Power Electron.*, vol. 4, no. 4, pp. 1383–1396, Dec. 2016.

Lei Gao (Student Member, IEEE) received the M.Eng. degree in electrical engineering from North China Electric Power University, Beijing, China, in 2022. He is currently working toward the Ph.D. degree in electrical engineering with Shanghai Jiao Tong University, Shanghai, China.

His research interests include oscillatory stability of offshore wind farms integration via MMC-HVDC and online stability assessment and active suppression of wideband oscillations in renewable power systems.

Jing Lyu (Senior Member, IEEE) received the M.Eng. and Ph.D. degrees in electrical engineering from Shanghai Jiao Tong University, Shanghai, China, in 2011 and 2016, respectively.

From 2016 to 2017, he was a Postdoctoral Research Fellow with the Department of Engineering Cybernetics, Norwegian University of Science and Technology, Trondheim, Norway. Since 2018, he has been with the Department of Electrical Engineering, Shanghai Jiao Tong University, where he is currently a tenured Associate Professor. His research interests include dynamic stability of power electronic based power systems, wind power generation, HVDC transmission, and application of artificial intelligence in stability of renewable power systems.

Aolin Shi received the B.Eng. degree in electrical engineering in 2023 from Shanghai Jiao Tong University, Shanghai China, where he is currently working toward the M.Eng. degree in electrical engineering.

His research interests include impedance modeling and stability analysis of Grid-forming based MMC.

Xiaoqiang Fu is currently working toward the M.Eng. degree in electrical engineering with the School of Electrical Power Engineering, Shanghai University of Electric Power, Shanghai, China.

His research interests include impedance modeling and stability analysis of GFM-based and GFL-based MMC.

Xu Cai (Senior Member, IEEE) received the B.Eng. degree in electrical engineering from Southeast University, Nanjing, China, in 1983 and the M.Eng. and Ph.D. degrees from China University of Mining and Technology, Jiangsu, China, in 1988 and 2000, respectively, both in electrical engineering.

He was with the Department of Electrical Engineering, China University of Mining and Technology, as an Associate Professor from 1989 to 2001. He was the Vice Director of the State Energy Smart Grid R&D Center, Shanghai, China, from 2010 to 2013. Since 2002, he has been as a Professor with Shanghai Jiao Tong University, Shanghai, where he has also been the Director of the Wind Power Research Center since 2008. His research interests include wind power generation and grid integration, HVDC transmission, and high-power battery storage systems.